MECHANICAL CHARACTERIZATION AND CONSTITUTIVE MODELING OF HIGH-TEMPERATURE FLUOROELASTOMERS

Thesis

Submitted to

The School of Engineering of the

UNIVERSITY OF DAYTON

In Partial Fulfillment of the Requirements for

The Degree of

Master of Science in Mechanical Engineering

By

Brent Matthew Johnson

Dayton, Ohio

December, 2023

University of Dayton

MECHANICAL CHARACTERIZATION AND CONSTITUTIVE MODELING OF HIGH-TEMPERATURE FLUOROELASTOMERS

Name: Johnson, Brent Matthew

APPROVED BY:

Robert L. Lowe, Ph.D.
Advisory Committee Chair
Associate Professor, Mechanical and
Aerospace Engineering

Donald A. Klosterman, Ph.D.
Committee Member
Associate Professor and Torley Endowed
Chair, Chemical and Materials
Engineering

Thomas J. Whitney, Ph.D.
Committee Member
Associate Professor, Civil &
Environmental Engineering and
Engineering Mechanics

Allyson Cox, M.S.
Committee Member
Research Engineer, University of Dayton
Research Institute

Chad Jones, M.S.
Committee Member
Research Engineer, Maverick
Corporation

ABSTRACT

MECHANICAL CHARACTERIZATION AND CONSTITUTIVE MODELING OF HIGH-TEMPERATURE FLUOROELASTOMERS

Name: Johnson, Brent Matthew
University of Dayton

Advisor: Dr. Robert L. Lowe

Fluoroelastomers can maintain their stretchability and elasticity at high temperatures, making them well-suited for applications that require extreme thermal resistance. Presently, there is significant interest in casting compounded fluoroelastomers to create high-temperature seals with intricate geometric features. It is not well understood, however, how these materials will perform mechanically in service as they undergo repeated heat cycling and are subjected to complex, multi-axial stress states. To address this research opportunity, a suite of commercially available compounded fluoroelastomers were thermally aged (10, 20, 50 cycles at 200 °C for 8 hours) and mechanically tested in uniaxial tension and uniaxial compression. Preliminary room-temperature uniaxial tension results displayed increases in strength and elastic modulus with modest heat cycling (20 cycles), followed by a subsequent decrease in strength at large amounts of heat cycling (50 cycles). Even at 50 cycles, however, the heat-conditioned materials still exhibited greater strength than the unconditioned materials. This mechanical response is likely due to a competition between the chemical mechanisms of polymer cross-linking and chain scission, with strength degradation at large amounts of heat cycling reflective of chain scission dominating cross-linking.

From this suite of candidate materials, the compounded commercial fluoroelastomer FKM Viton A-500 RB75A5 was downselected for the desired sealant application and subsequently tested at elevated temperatures (85, 140, 200 °C) in uniaxial tension to better understand its behavior in extreme

environments. Lower mechanical strength and reduced elongation were observed in the material's elevated temperature response. This is likely because the higher temperatures result in shorter polymer chains, which corresponds to a higher entropy state and a weaker, lower-elongation material. Additional room-temperature tests were performed on Viton RB75A5 to facilitate the calibration of hyperelastic constitutive models, both parameterized (e.g., Ogden) and tabulated. Coupon-level validation tests involving inhomogeneous planar deformations were used to verify the accuracy of the constitutive models. Comparisons of principal surface strains from digital image correlation to LS-DYNA finite element simulations of the tests indicate that the tabulated (MAT_181) and parameterized Ogden models capture the inhomogeneous deformation well. These validated material models for unconditioned Viton RB75A5 can be used for simulation-aided design and optimization of seals and other elastomeric components.

ACKNOWLEDGMENTS

I would like to express gratitude to Dr. Robert Lowe for the opportunity to work in the Behavior of Advanced Materials and Structures (BAMS) Lab, and for his mentorship throughout my graduate studies and research. I appreciate his guidance over the past two years and am thankful for the knowledge and skillset I have gained through him.

I would also like to acknowledge the United States Air Force for funding this research. I have learned a lot from the engineers at the University of Dayton Research Institute (UDRI) and Maverick Corporation, and I would especially like to thank Ally Cox, Chad Jones, and Tim Osborn for their guidance and consultation throughout my research program. I enjoyed working with the Additive Manufacturing Technology Development (AMTD) team and am thankful to have learned from them. I would also like to thank Braeden Windham and Nate Maleski for their work in fixture development for the BAMS Lab, giving me more testing capabilities in my research. Anthony Bazler and Ryan McGill were extremely helpful in helping me learn and understand methods in digital image correlation. There are endless others I could thank at UDRI for their guidance and resources.

I would also like to thank Dr. Donald Klosterman for providing insight and knowledge into the polymer science behind the material behavior I have researched, and also for sharing his lab resources. Dr. Thomas Whitney has also been a great source of knowledge in solid mechanics. I am thankful for Dr. Elias Toubia and the Department of Civil and Environmental Engineering and Engineering Mechanics for allowing me to use their Correlated Solutions VIC-2D license. Luke Hoover (ANSYS) has provided excellent support in helping me learn LS-DYNA.

Hannah Kolkmeyer inspires me to be the best I can be, and I would not be where I am today without her. I would also like to thank her for her endless love, support, and selflessness. She is the

most amazing woman I know, and I am thankful to have her in my life. I also am appreciative of the support her family has provided me in the past couple of years.

Thank you to all of my friends back home and also to Luke, Kyle, and Eddie for their friendship through graduate school. Thank you also to the all members of the BAMS Lab who have provided significant support and have made every day entertaining. Aimable, Eddie, Ethan, Grant, Reed, and Yatik especially were there for the majority of my time in graduate school, and have made the experience and culture in the lab.

I cannot thank my family enough for the love and support they have given me. My siblings Ryan, Eric, and Ashlyn have given me endless support throughout my life, and I am grateful to have them. Ryan and Eric are outstanding role models that I have always looked up to, and Ashlyn is the best little sister I could ask for. I am proud of Ryan for his accomplishments as a software engineer, Eric who recently just became a certified financial planner, and Ashlyn who plans to pursue a career in occupational therapy. I would also like to thank Grandma J and Grandma C for their mental support all these years. My hard work and studying were often fueled by the cookie-care packages Grandma C would send me. Most of all I would like to thank my parents, Mike and Dawn, for their endless love and support, and for always being there for me. I am so thankful for them and appreciate them encouraging me to pursue my graduate degree.

VITA

May 2018	Diploma, Father Gabriel Richard High School, Ann Arbor, MI
May 2022	Bachelor of Science in Mechanical Engineering, University of Dayton, Dayton, OH
May 2022-Present	Graduate Research Assistant, Behavior of Advanced Materials and Structures Lab, University of Dayton, Dayton, OH

PUBLICATIONS

1. S. Wanasinghe, **B. Johnson**, R. Revadelo, G. Eifert, A. Cox, J. Beckett, T. Osborn, C. Thrasher, R. Lowe, and D. Konkolewicz. 2023. 3D Printable Adhesive Elastomers with Dynamic Covalent Bond Rearrangement. Soft Matter 19(26), 4964-4971.

2. **B. Johnson**, C. Jones, A. Cox, T. Osborn, R. Lowe. Mechanical Characterization and Constitutive Modeling of High-Temperature Fluoroelastomers. In progress; to be submitted.

PRESENTATIONS

1. **B. Johnson** (presenter), A. Cox, C. Jones, R. Gray, T. Osborn, R. Lowe, “Mechanical Characterization of High-Temperature Fluoroelastomers,” 49th Dayton-Cincinnati Aerospace Sciences Symposium (AIAA DCASS 2023), Dayton, OH.

2. **B. Johnson** (presenter), A. Cox, C. Jones, R. Gray, T. Osborn, R. Lowe, “Mechanical Characterization of and Constitutive Modeling of High-Temperature Fluoroelastomers,” International Mechanical Engineering Congress and Exposition (ASME IMECE 2023), New Orleans, LA.

TABLE OF CONTENTS

APPENDICES

LIST OF FIGURES

LIST OF TABLES

LIST OF VARIABLES AND CONSTANTS

- ε_{eng} - Engineering Strain (mm/mm or %)
- L_0 - Original Length (mm)
- ΔL - Change in Length (mm)
- c - Material Constant for Mooney-Rivlin Model
- α - Material Constant for Ogden Model
- μ - Material Constant for Ogden Model
- T_0 - Stress Tensor (MPa)
- λ - Stretch

LIST OF ACRONYMS

- DIC - Digital Image Correlation
- FEA - Finite Element Analysis
- VE - Virtual Extensometer
- VSG - Virtual Strain Gage
- UTS - Ultimate Tensile Strength
- FLIR - Forward Looking InfaRed
- CAD - Computer Aided Design
- FKM - Fluorine Kautschuk Material

CHAPTER I

INTRODUCTION

1.1 Background and Applications

High-temperature fluoroelastomers have gained significant attention recently, encompassing a class of polymers capable of withstanding extreme thermal environments. Fluoroelastomer blends (FKM) possess attractive mechanical properties, chemical resistance, and extreme thermal stability [1]. As a result, high-temperature fluoroelastomers have emerged as a compelling solution to the demand for high-performance elastomers in aggressive chemical and thermal environments.

Fluoroelastomers are polymers that contain fluorine atoms within their chemical structures, either as perfluoropolymers or partially fluorinated polymers [2]. The highly electronegative fluorine bond is very difficult to break, contributing to the overall strength and durability of fluoropolymers. Fluoropolymers have exceptional chemical resistance, thermal stability, and low surface energy, due to their unique molecular interactions in fluorinated polymer segments and main chains [2]. The fluoropolymer's chemistry was derived from fluorocarbon compounds initially developed for refrigerants [3]. The creation of polytetrafluoroethylene (PTFE; 1.1) in the 1930s sparked the development of fluorinated thermoplastics and elastomeric fluorine-containing polymers [3].

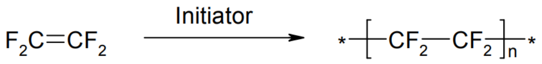

$$F_2C{=}CF_2 \xrightarrow{\text{Initiator}} *\!-\!\left[CF_2-CF_2\right]_n\!-\!*$$

Figure 1.1: Polymerization of TFE [2]

A variety of fluoropolymers such as polychlorotrifluoroethylene (PCTFE), fluorinated ethylene propylene (FEP), and polyvinylfluoride (PVF) were later developed in the 1950s and 1960s [2].

Dyneon THV (Figure 1.2) was developed in the 1990s, which has excellent permeation resistance and chemical resistance and is well-suited for applications that demand significant stretchability and flexibility [2].

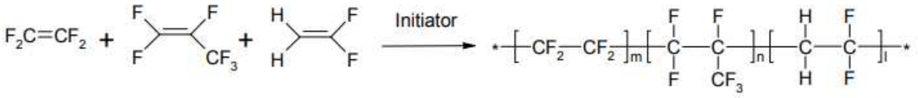

Figure 1.2: Polymerization of THV [2]

There is a significant need for synthetic, rubber-like materials capable of surviving extreme environments in the oil and gas industry [4]. Elastomeric materials in this industry are frequently used for static and dynamic sealing between mechanical components, but high temperatures frequently reduce the elongation and bulk modulus of rubbers [4]. Fluoroelastomers retain their mechanical properties at high temperatures and thus have also found widespread use in the aerospace, automotive, and semiconductor manufacturing sectors. Thread sealant tape, for example, leverages the exceptional properties of fluoroelastomers to enable highly durable and reliable performance in sealed joints [3]. These high-temperature materials are also commonly used for O-rings or bulb seals (Figure 1.3), aiding the performance of manufacturing equipment, chemical processing plants, and engines. These seals can outperform silicone elastomers, which cannot be used in extreme environments.

Figure 1.3: Finite element simulation of a bulb seal in compression

Fluoroelastomers can even be used for the fabrication of Viton-based microfluidics by micromoulding, bonding, and metal patterning [5]. Fluoroelastomers often provide manufacturing solutions to the automotive and aerospace industries because they provide excellent thermal stability for equipment subjected to extreme temperatures and pressure changes [3]. While there are risks to the fluoropolymer industry at the moment, due to increasing regulations on manufacturing and emissions, there is also room for growth as they are utilized in a variety of emerging industries such as the electric vehicle industry.

To predict the deformation of elastomers in complex stress states and extreme environments, accurate material models (i.e., constitutive models) are needed to capture how the material responds under various loading conditions. To indeed be accurate and truly predictive, these constitutive models must be calibrated using high-quality experimental data. This experimental data is typically generated through coupon-level testing across diverse stress states (e.g., uniaxial tension, uniaxial compression, simple shear, and pure shear). These tests provide insight into the material behavior under complex stress states before failure and enable the calculation of key mechanical properties such as elastic modulus, ultimate tensile strength, elongation at break, and toughness. Additional testing is often performed to assess the importance of viscoelastic effects (e.g., stress relaxation, creep, cyclic, and rate sensitivity) and thermal sensitivity (e.g., low/high-temperature tests). With this data, nonlinear least squares curve fitting can be performed to calibrate constitutive models. These constitutive models can then be used in finite element software (e.g., Ansys LS-DYNA) for predictive stress analysis on three-dimensional parts and components. Accurate material models thus enable simulation-aided prototyping, design, and optimization, thereby reducing material waste, time for physical testing, and equipment costs. Within this investigation, LS-DYNA is chosen as the finite-element solver for all stress analysis.

1.2 Literature Review

1.2.1 Mechanical characterization of elastomers

Elastomers exhibit complex nonlinear response that depends on their intrinsic polymer chemistry, composition, and processing. As such, each material must be tested individually to understand its unique mechanical performance. The response of elastomers can also be impacted by extrinsic factors such as stress state, temperature, humidity, loading rate, and thermal aging.

Numerous experimental efforts have been undertaken that attempt to fundamentally understand the influence of these factors on mechanical response. In the seminal work of Treloar [6], the quasi-static response of a vulcanized rubber was investigated under uniaxial tension, equi-biaxial tension, and pure shear. The influence of stress state on mechanical response was also explored by Meunier et al. [7], who characterized a silicone rubber in uniaxial tension, uniaxial compression, pure shear, and plane strain compression. Simple (lap) shear testing has been performed on PDMS [8, 9], silane-modified elastomers [10], and self-healing elastomers [11], for example. A useful collation of experimental methods for elastomers is presented in the book by Brown [12]. The methods within this thesis are inspired by previous research done in references [6–12], where elastomers are tested in a variety of stress states, often for the purpose of constitutive model calibration.

In recent years, non-contact optical strain measurement methods such as digital image correlation (DIC) have been developed. This technique captures the motion of a randomly applied, high-contrast speckle pattern applied to a specimen. Specialized DIC software is then used to correlate the camera images and calculate full-field measurements of the surface strains (often visualized using contour plots) throughout the test. Virtual extensometers (VE) and virtual strain gages (VSG) are placed using built-in tools in the software, which allow for strain to be interrogated at specified areas within the test coupon. DIC has been used in previous research for both calibration experiments (e.g., uniaxial tension testing) and validation experiments (e.g., component-level tests, or tension tests on specimens with through-holes) [7]. During uniaxial tensile testing, the strain field in the gage section is nearly homogeneous until fracture. Near the onset of fracture, there is a slight localization, where the VSG can be utilized to measure the strain at the point of fracture. The same strategy can be used in validation testing, as the localized strains within the validation coupon can be compared in parallel to finite element simulation to validate the constitutive model. DIC methods allow for strain calculations at these localized areas, which are not obtainable through optical or clip-on extensometers.

1.2.2 Constitutive modeling of elastomers

Numerous hyperelastic constitutive models have been proposed in the literature to describe the nonlinear elastic response of rubbers, elastomers, and soft materials. Common examples include the neo-Hookean model [13], the Mooney-Rivlin model [14], the Gent model [15], the Yeoh model [16], the Arruda-Boyce model [17], and the Ogden model [18, 19]. Recent reviews of hyper-elastic material models are provided by Steinmann and Hossain [20, 21]. Among these, the incompressible

Ogden model [18,19] is a popular hyperelastic constitutive model. In uniaxial tension, the engineering stress-stretch relationship for the Ogden model is described by the following equation, where T_0 is the engineering stress, λ is the stretch, and μ and α are material constants:

$$(\mathrm{T}_0)_{11} = \mu_1\left(\lambda^{\alpha_1-1} - \lambda^{-\frac{1}{2}\alpha_1-1}\right) + \mu_2\left(\lambda^{\alpha_2-1} - \lambda^{-\frac{1}{2}\alpha_2-1}\right) + \mu_3\left(\lambda^{\alpha_3-1} - \lambda^{-\frac{1}{2}\alpha_3-1}\right) \tag{1.1}$$

The material constants are calibrated by fitting 1.1 to uniaxial tension test data.

Three constitutive models, all natively built into the LS-DYNA hyper-elastic material library, were chosen for this investigation – two parameterized (Mooney-Rivlin, MAT_027 and Ogden, MAT_077) and one tabulated (MAT_181). It is well known that the Mooney-Rivlin model overestimates the stress response to stretch [20]. A disadvantage of the Ogden model is that it cannot reproduce an exact fit of the test data due to the least-squares method requiring monotonically increasing smooth data. A tabulated approach to hyper-elastic constitutive modeling in LS-DYNA (MAT_181) has been used to simulate the mechanical behavior of rubber [22, 23]. This model requires uniaxial response only, whereas testing across multiple stress states is recommended for the Ogden model. The MAT_181 model allows direct importation of load curves into the software [22,23], and has built-in options for incorporating visco-hyperelastic effects [22]. As a result, with the MAT_181 model, strain-rate dependence and Mullins effect (damage parameter) can be modeled. Other constitutive developments also include these advanced physics, including viscoelasticity [24], the Mullins effect [25–27,40], temperature dependence [38], and thermal aging [28].

1.2.3 Characterization and constitutive modeling of fluoroelastomers

When experimentally characterizing fluoroelastomers, it is important to consider intrinsic (chemistry, composition, and processing) and extrinsic (stress state, temperature, humidity, loading rate, and thermal aging) factors that can impact mechanical performance. For instance, the effect of oven post-cure (thermal aging) Viton materials is explained by the formation of crosslinks accompanied by the elimination of hydrogen fluoride (HF) from the polymer [29]. Kalfayan discusses the effects of chain scission and cross-linking in vulcanized fluorocarbon rubbers exposed to thermal aging [30]. More recent studies have explored volume resistivity measurements of fluoroelastomers after thermal aging [31]. SEM micrographs of a virgin sample (c1) and a sample submerged in water and thermally aged for 100 hr at 225 °C (c2) are shown in Figure 1.4. This work shows large cracks on aged samples resulting in decreased resistivity initially, but proposes that as temperature increases, more moisture evaporates leading to less moisture in the cracks. As a result, the difference in resistivity between new and aged samples is reduced. This thesis expands on this previous work, further exploring the competing effects of chain scission and cross-linking as fluoroelastomers are thermally aged.

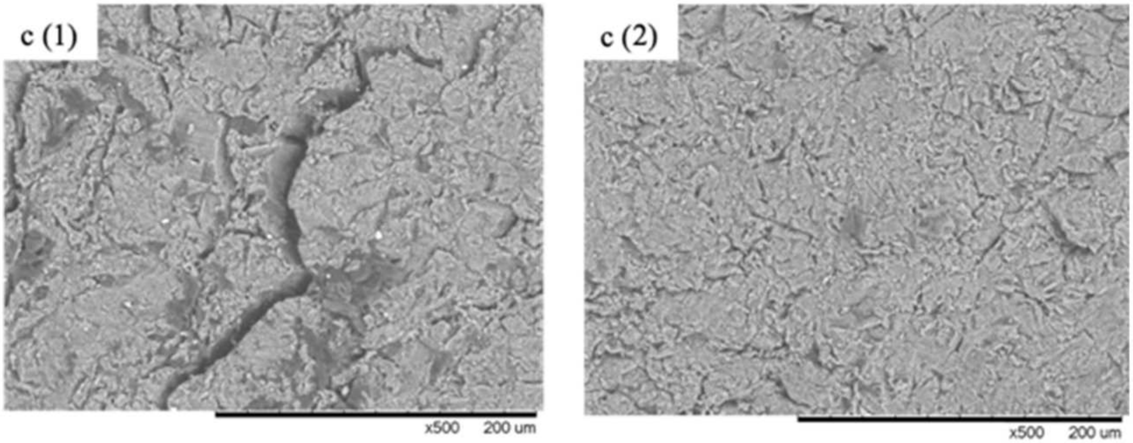

Figure 1.4: SEM micrographs of a virgin and aged Viton sample at x500 magnification (c1) aged sample (c2) virgin sample [31]

Wang and Chester [24] investigated the viscoelastic and stress-softening behavior of similar Viton materials, as seen in Figure 1.5. In these results, there is a visible Mullins effect and rate-dependent behavior (Figure 1.5a), as well as inelasticity and asymmetry in the loading/unloading profiles (Figure 1.5b). This thesis expands on [24], incorporating findings from [30] to investigate the competition in viscoelastic and thermal effects.

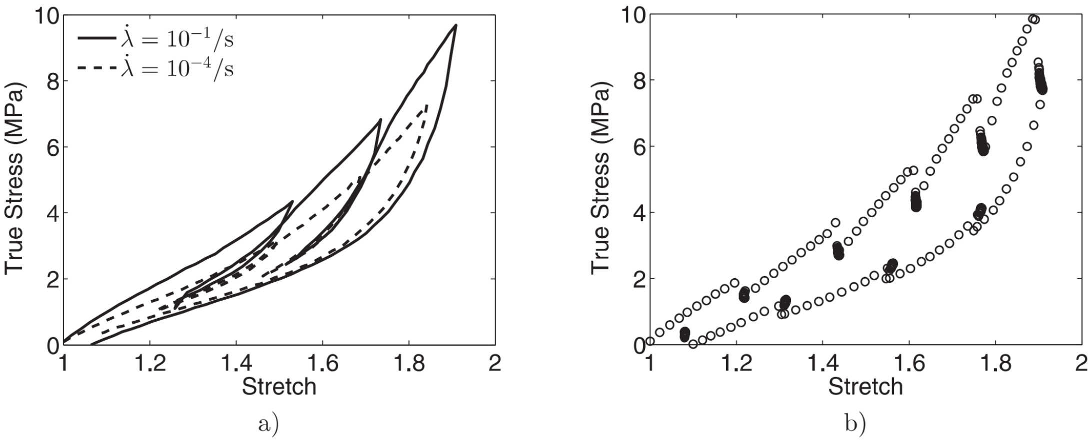

Figure 1.5: Uniaxial tensile tests on independent specimens of virgin Viton. (a) Load/unload/reload test results at two different stretch rates, and (b) multi-step stress relaxation test results [24]

1.3 Research Opportunity, Objectives, Scope, and Novelty

There are well-known pros and cons in the capabilities and convenience of the constitutive models to be used herein. However, there are only limited investigations exploring how parameterized (e.g., Ogden, MAT_077) and tabulated (e.g., MAT_181) constitutive models compare in predicting complex stress states. This research expands on previous literature by comparing the accuracy of the Mooney-Rivlin, Ogden, and LS-DYNA's tabulated MAT_181 constitutive models in replicating complex deformations.

Understanding and characterizing the mechanical properties of fluoroelastomers is essential in understanding how they will endure mechanical stress, resist deformation, and maintain their functionality over time within complex designs and in harsh environments. There is limited research, however, on how compounded fluoropolymer materials behave after thermal aging or in diverse stress states. There is a need for a deeper understanding and characterization of fluoroelastomers to anticipate how they will endure stress, resist deformation, and maintain their functionality over time with complex designs and in harsh environments. There is a need to understand how these harsh environments affect the mechanics of these materials. Trustworthy mechanical test data can provide insight into the deformation of these materials in different loading conditions in different environments.

Chapter 2 details the mechanical characterization of a set of thermally aged flouroelastomers, to anticipate how they will perform in the desired application's extreme thermal environment. From Chapter 2, a single material will be selected (based on optimal properties) for the sealant application and for further characterization in Chapter 3. Chapter 3 delves into viscoelasticity, strain-rate dependence, and response under multiple stress states (uniaxial tension, uniaxial compression, pure shear, simple shear). Chapter 3 also involves constitutive modeling and finite-element validation for the selected material. The significance of material processing conditions is stressed throughout both chapters, as the material performance is sensitive to a variety of processing conditions. The resulting mechanical test data and constitutive models can be utilized in predictive computational models.

CHAPTER II

DOWNSELECTION OF PROSPECTIVE FLUOROELASTOMERS

2.1 Introduction

Mechanical testing in quasi-static uniaxial tension and uniaxial compression was used to evaluate potential fluoroelastomer sealant materials. To best represent the operating environment of a seal that is used in service in the target application, materials were heat cycled (thermally aged) for 8 hours at 200 °C with a varying number of cycles prior to tension and compression testing.

2.2 Materials, Specimen Preparation, and Experimental Methods

Six fluoroelastomers were investigated as potential sealant materials. Three were derivatives of the commercial fluoroelastomer Dyneon FPO 3600 ULV (3M) with 10, 20, and 30 phr carbon black (Thermax N990, Cancarb), compounded by 3M. The Dyneon-based compounds were prepared using a two-roll lab mill and contained raw Dyneon gum rubber, carbon black filler, crosslinker (triallyl isocyanurate), and a peroxide-based accelerator. The other three materials were derivatives of the commercial fluoroelastomer Viton (Chemours), a copolymer of hexafluoropropylene and vinylidene fluoride. Three custom Viton-based compounds were prepared by the supplier using varying amounts of carbon black filler, curing agents, and other processing aids (formulations RB65A5, RB75A5, and RB75GF5; Rainbow Master Mixing).

The Dyneon tension specimens used for material evaluation were die cut from a 3-mm-thick sheet that was compression molded (152.4 x 152.4 x 3 mm mold) at 160 °C for 8 min. No post-curing was done with the Dyneon (prior to thermal aging). The Viton sheets were compression molded at 176.7 °C for 10 min into 2-mm-thick rectangular sheets and post-cured for 16 hr at 232 °C (prior to any thermal aging). The tension specimens for all materials were cut using an

ASTM D412 type C die, and the compression specimens were provided by the supplier (Rainbow Master Mixing) following similar processing and fabrication methods. The test specimens were then thermally aged under various numbers of heat cycles (Tables 2.1 and 2.2), where each heat cycle consisted of ramping up to 200 °C, holding at 200 °C for 8 hr, and ramping down to 25 °C.

The test matrices created and executed for initial material downselection for tension (Table 2.1) and compression (Table 2.2) are shown below, displaying the number of specimens tested for each material and heat cycle combination. Quasi-static tension and compression results of the material variations were used to assess suitability for the intended application and to aid in selecting the top candidate(s) for full characterization.

Table 2.1: Initial material evaluation – Tension testing

Material	Virgin	10 Cycles	20 Cycles	50 Cycles
Dyneon 10 phr	-	-	3	-
Dyneon 20 phr	-	-	6	-
Dyneon 30 phr	4	-	4	3
Viton RB65A5	5	5	5	5
Viton RB75A5	5	5	5	5
Viton RB75GF5	5	5	5	5

Table 2.2: Initial material evaluation – Compression testing

Material	Virgin	10 Cycles	20 Cycles	50 Cycles
Viton RB65A5	5	5	5	5
Viton RB75A5	5	5	5	4
Viton RB75GF5	5	5	5	5

All quasi-static tension tests were conducted under ambient conditions in accordance with ASTM D412 (Standard Test Methods for Vulcanized Rubber and Thermoplastic Elastomers — Tension) [32]. Cross-sectional measurements of all original, undeformed specimens were made with a digital Mitoyo caliper. An Instron 3365 extended-height, screw-driven universal testing machine with pneumatic side-action tensile grips was used to load the specimens (Figure 3.3). The crosshead was actuated at 50 mm/min to ensure nearly quasi-static loading conditions. The load frame was equipped with a 2-kN load cell and recorded engineering strain using a clip-on extensometer. The extensometer measures the length change ΔL during testing between two points in the gage section initially separated by a distance $L_0 = 25.4$ mm. The instantaneous length change ΔL is normalized by the characteristic length L_0 to provide the axial engineering strain $\varepsilon_{eng} = \Delta L/L_0$. Within this length-averaged measurement is the deformation in the gage section (within the extensometer window), which is nearly homogeneous to fracture.

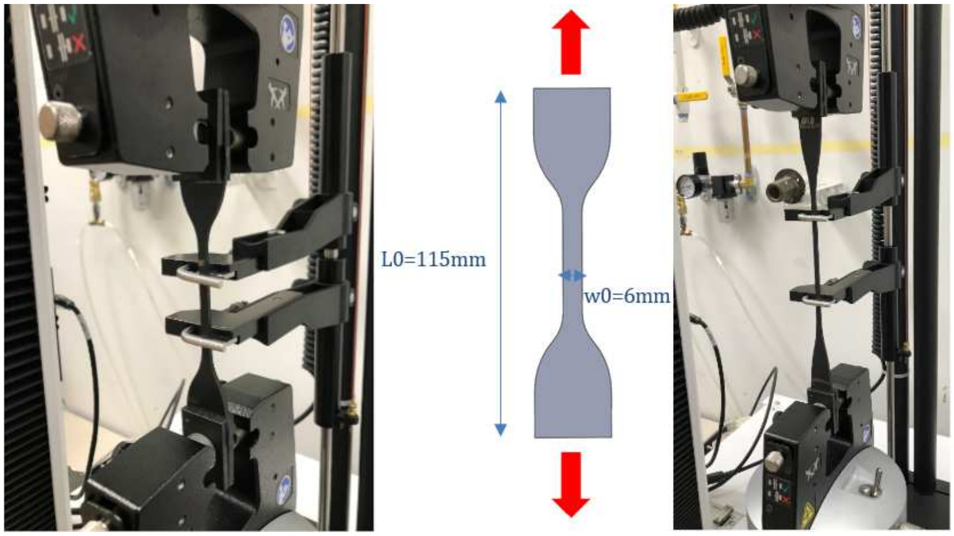

Figure 2.1: Uniaxial tension testing

Quasi-static compression tests were conducted in accordance with ASTM D575-91 (Standard Test Methods for Rubber Properties in Compression) [33] on an Instron 3365 universal testing machine under ambient conditions using custom compression platens. Tests were performed with the crosshead moving at a constant rate of 12.5 mm/min. Compression samples differed from the standard, measuring only 6-7 mm in height. Cross-sectional measurements of all original, undeformed specimens were made with a digital Mitoyo caliper. The test machine was equipped with a 5-kN load cell for force measurement. Engineering strain was calculated using the crosshead displacement (measured by the built-in LVDT) divided by the original height of the test specimen. Engineering stress was calculated as force divided by the original cross-sectional area.

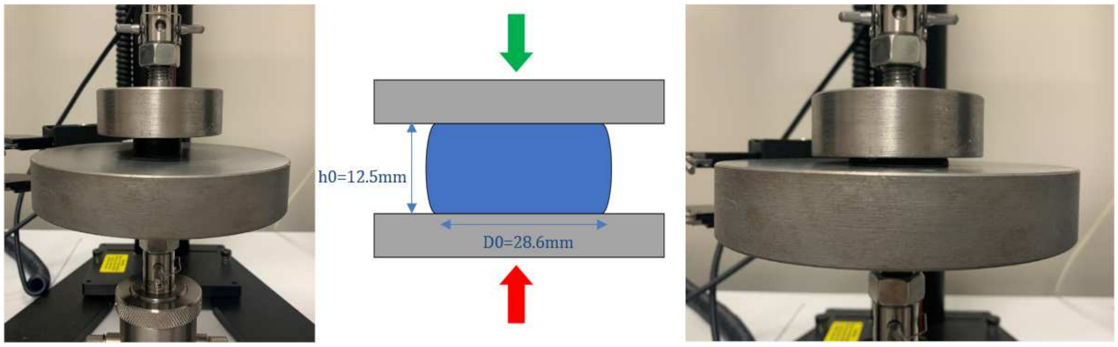

Figure 2.2: Uniaxial compression testing

2.3 Experimental Results

Heat-cycled Dyneon FPO 3600 ULV (20 cycles) with varying concentrations of carbon black was evaluated in uniaxial tension (Figure 2.3). The 10 phr Dyneon had the lowest UTS and a high elongation (12.6 MPa, 258.9%). The 20 phr Dyneon had both the highest UTS and elongation (16.7 MPa, 260%). The 30 phr Dyneon had the lowest elongation and the second-highest UTS (15.9 MPa, 213%). Overall, increased carbon black content led to a stiffer stress-strain response, with the

20 phr Dyneon having optimum mechanical properties in strength and elongation for the desired application.

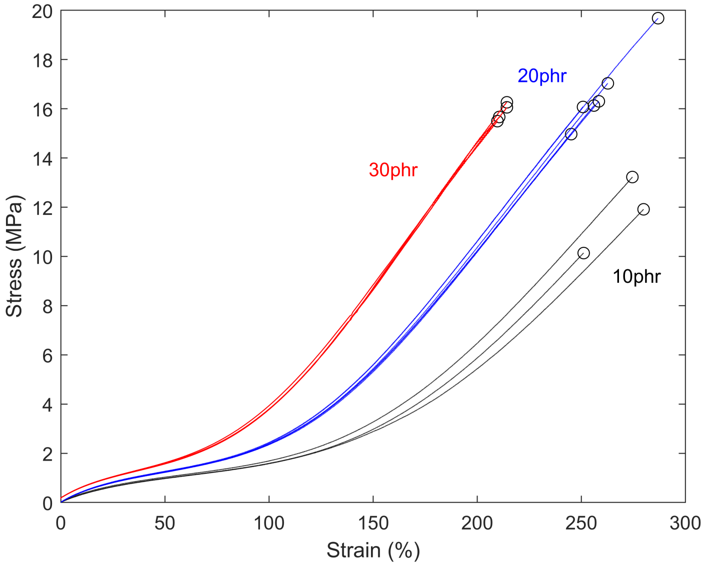

Figure 2.3: Uniaxial tension response of Dyneon with varying carbon black filler content (10, 20, 30 phr) subjected to 20 heat cycles

Figure 2.4 displays Viton RB65A5, RB75A5, RB75GF5, and Dyneon 30 phr across all tested levels of thermal conditioning in uniaxial tension. It is seen in Figure 2.4d that there was a significant increase in strength when the material was conditioned for 20 cycles. When the thermal conditioning increased to 50 cycles, there was a decrease in strength. Although there was a decrease at 50 cycles, the material was still significantly stronger than the virgin material. This mechanical response was likely due to a competition between the chemical mechanisms of polymer cross-linking and chain scission, with strength degradation at large amounts of heat cycling reflective of chain scission dominating cross-linking. The same trends were observed for the thermally aged Viton variants (Figure 2.4), although the changes in mechanical properties were less notable. This indicates that the heat treatment had a less significant impact on the Viton, but the same underlying chemical processes were still occurring and driving the macro response.

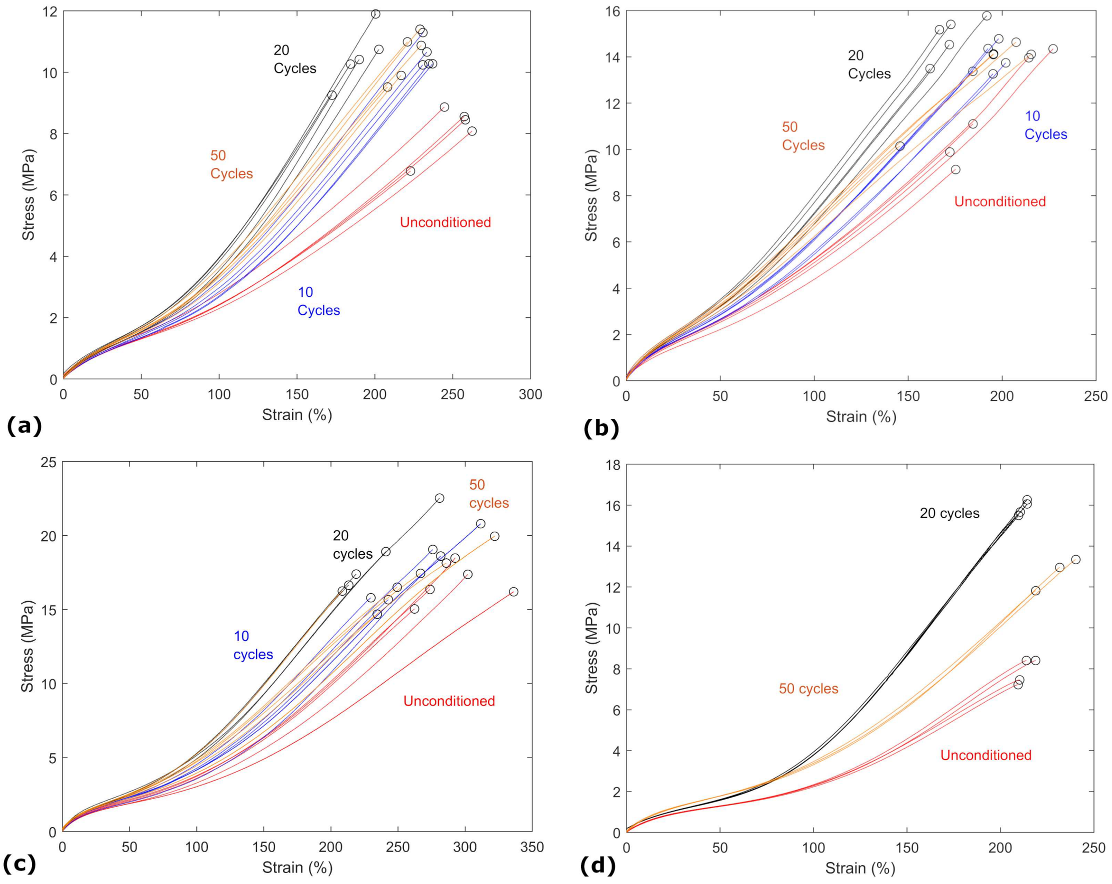

Figure 2.4: Uniaxial tension response of (a) Viton RB65A5, (b) Viton RB75A5 (c) Viton RB75GF5, and (d) Dyneon 30 phr after 0, 10, 20, and 50 heat cycles.

Viton materials were compared to 10, 20, and 30 phr Dyneon after all materials were thermally aged for 20 cycles (Figure 2.5). The ultimate tensile strength of the RB75A5 (14.9 MPa) compared most closely to the 30 phr Dyneon (15.9 MPa) and 20 phr Dyneon (16.7 MPa). These quantities, however, are not fully indicative of the mechanical behavior of the materials. For instance, as shown in Figure 2.5b, the early mechanical behavior, i.e., the first 100% strain window, is most similar between the RB65A5 (one-percent Young's modulus of 6.3 MPa), 30 phr Dyneon (two-percent Young's modulus of 5.5 MPa), and the 20 phr Dyneon (one-percent Young's modulus of 5.6 MPa). In this early portion of the stress-strain curve, the RB75A5 responds more stiffly than the Dyneon materials.

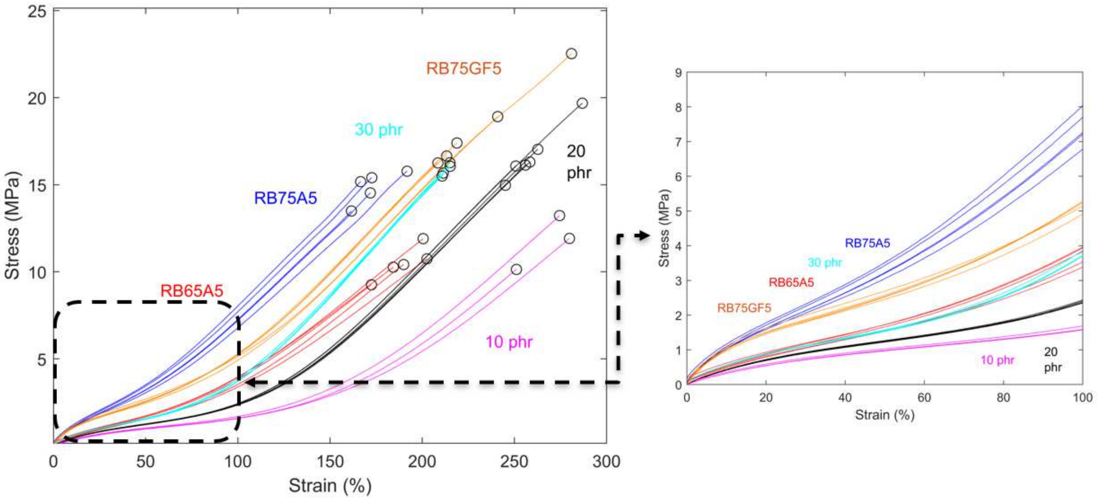

Figure 2.5: (a) Uniaxial tension response of all six material candidates after 20 heat cycles (a) until fracture and (b) up to 100% strain.

In addition to tension testing, compression testing was performed to aid in material selection. Due to limited material availability, only the three Viton derivatives were evaluated. Figure 2.6 shows the effect of heat cycling on the compressive response of each Viton-based material. Note that the maximum stress in these tests does not correlate with specimen fracture, but rather the stress at which the load cell reached its upper limit of 5 kN. Similar to the tension results, the material responds more stiffly after 20-50 cycles of thermal aging.

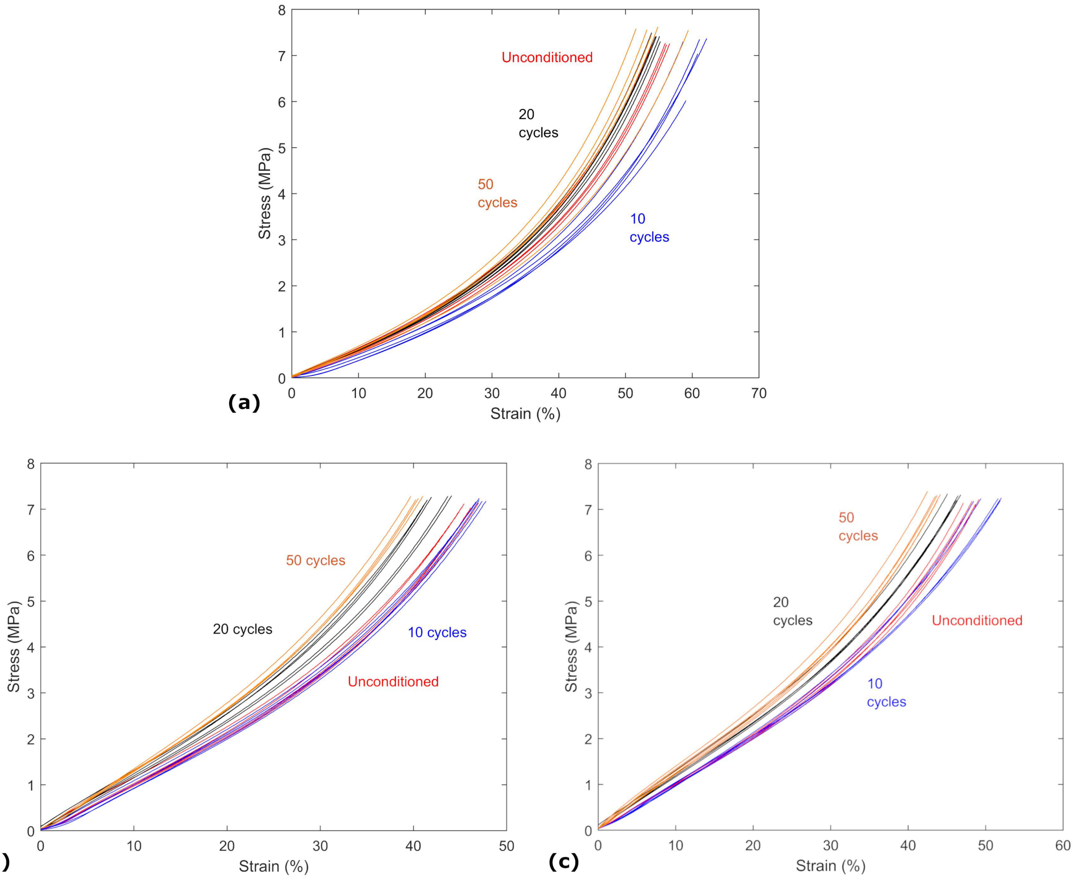

Figure 2.6: Uniaxial compression response of Viton (a) RB65A5, (b) RB75A5, and (c) RB75GF5 after 0, 10, 20, and 50 heat cycles.

Figure 2.7 shows the compressive response of each Viton derivative after various levels of thermal aging. The virgin RB65A5 compressive results displayed a greater elongation (55.3%) at a 5 kN load and a lower compressive modulus (5.0 MPa). The unconditioned RB75A5 showed the same compressive modulus (5.0 MPa) and lower elongation (46.0%) at a 5 kN load. The unconditioned RB75GF5 also resulted in a greater compressive modulus (6.7 MPa) and lower elongation (48.3%) at a 5 kN load. Similar trends are seen in the virgin, 10 cycle, 20 cycle, and 50 cycle tests. Overall, these results suggest that the RB75A5 and RB75GF behave more stiffly and are thus more resistant to compressive deformation than the RB65A5.

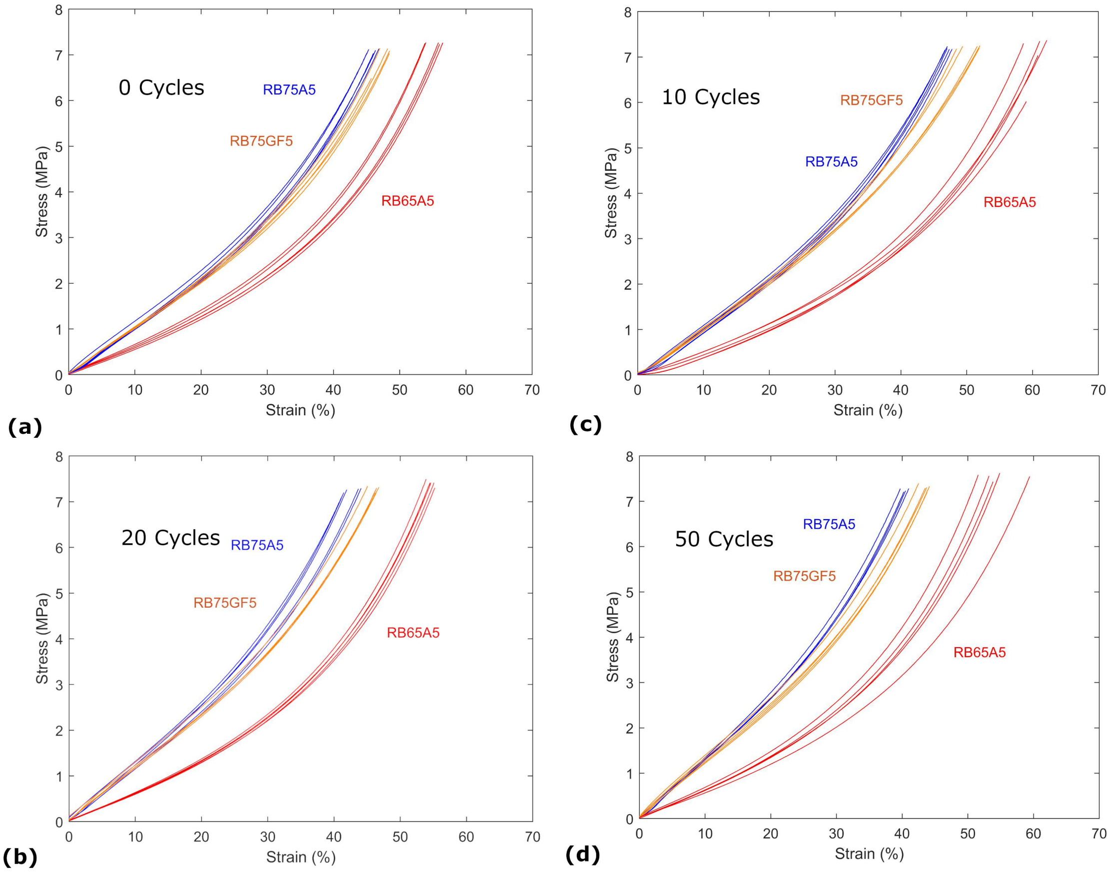

Figure 2.7: Uniaxial compression response of Viton RB65A5, RB75A5, and RB75GF5 after (a) 0, (b) 10, (c) 20, and (d) 50 heat cycles.

2.4 Conclusions

Among the Dyneon variants (10, 20, and 30 phr) subjected to 20 heat cycles, the 10 phr had the lowest UTS and high elongation, whereas the 20 phr had both the highest UTS and elongation. The 30 phr Dyneon had the lowest elongation and second highest UTS. Increased carbon black content led to a stiffer stress-strain response. Overall, the 20 phr Dyneon had the most desirable trade-offs among mechanical properties for the targeted application.

Tensile strength increased (across all materials investigated) after 20 heat cycles. When the thermal conditioning increased to 50 cycles, however, there was a decrease in strength. Although there was a decrease at 50 cycles, the material was still significantly stronger than the virgin material. This mechanical response was likely due to a competition between the chemical mechanisms of polymer cross-linking and chain scission, with strength degradation at large amounts of heat cycling reflective of chain scission dominating cross-linking. In compression testing, there was a similar trend of stiffer behavior after thermal aging.

The Viton RB65A5 was deemed most compatible with Dyneon materials for small strains, and the Viton RB75A5 was deemed most compatible with Dyneon materials at large strains. The Viton RB75A5 was ultimately selected due to the ease of processability for the sealant material. As a result, the RB75A5 was selected for full experimental characterization in Chapter 3.

CHAPTER III

CHARACTERIZATION, CONSTITUTIVE MODELING, AND FEA

3.1 Introduction

In this chapter, data from additional coupon testing in uniaxial tension, uniaxial compression, simple shear, and pure shear will be performed to fully characterize the downselected fluoroelastomer under a wide range of practically important stress states. The results of this additional testing will be used to calibrate hyper-elastic constitutive models for use in component-level finite element analysis (FEA) simulations of fluoroelastomer seals operating in service. The fidelity of the constitutive models will be validated through parallel experimental testing and FEA simulation of tension coupons with through-holes, which undergo complex inhomogeneous deformations.

3.2 Materials and Experimental Methods

3.2.1 Materials and specimen preparation

The material used in this investigation is a commercially available fluoroelastomer, Viton A-500 (Chemours), referred to as Viton RB75A5. Raw gum rubber, containing 66 wt% fluorine with a bisphenol-based curing agent, was custom compounded with carbon black filler and additional processing aids (formulation RB75A5, Rainbow Master Mixing). The resulting slab was compression molded at 176.7 °C for 10 min into 2-mm-thick rectangular sheets. No post-cure was performed after pressing.

Tension and pure shear samples (Figure 3.1a and Figure 3.1d) were cut from the sheet using tolerance-certified dies (Fremont Cutting Dies). Lap shear specimens (Figure 3.1c) were cut directly from the sheet using an ISDIR paper cutter. The compression specimens (Figure 3.1b) were provided directly by the supplier (Rainbow Master Mixing) following similar processing and fabrication methods. The dimensions of all original, undeformed specimens were measured using a digital Mitoyo caliper.

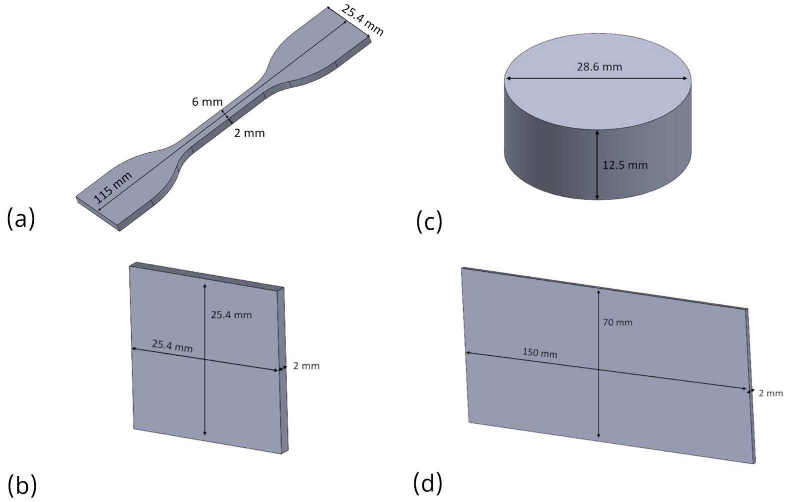

Figure 3.1: Test coupons: (a) tension, (b) simple shear, (c) compression, and (d) pure shear

In addition to samples that lead to simple homogeneous deformations (for constitutive model *calibration*), samples intended to elicit complex inhomogeneous deformations were prepared (for constitutive model *validation*). A custom tolerance-certified 25.4 mm × 50.8 mm (1 in. × 2 in.) die (Fremont Cutting Dies) was used to cut the footprint of the validation samples (Figure 3.2) from the sheet. After the outer geometry was cut, 7.9375 mm (0.3125 in.) and 3.9675 mm (0.1562 in.) diameter dies (from the same vendor) were used to punch the through-holes. The remaining specimen geometry dimensions are detailed in Table 3.1. As with the calibration coupons, the dimensions of all original, undeformed validation specimens were measured using a digital Mitoyo caliper.

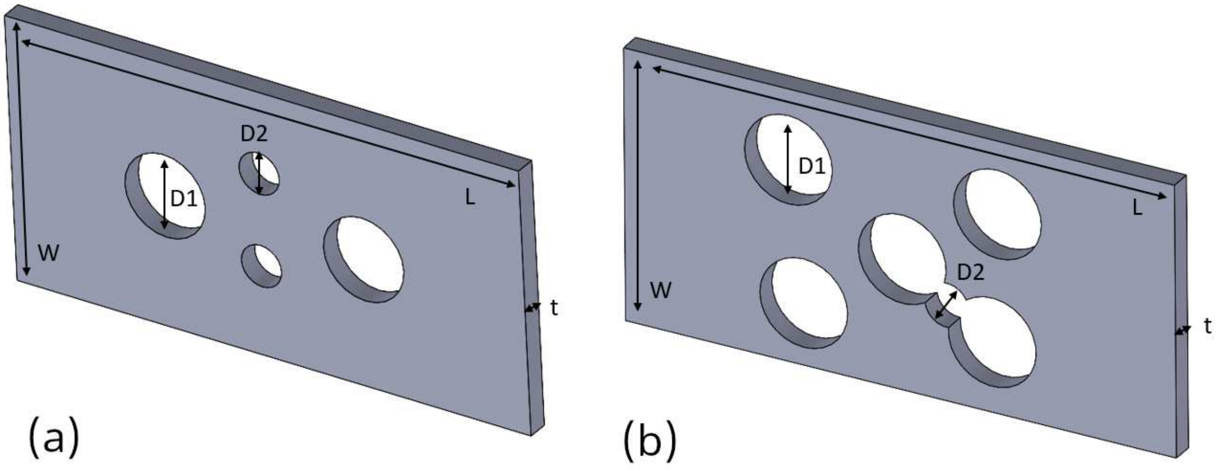

Figure 3.2: Validation coupons: (a) four-hole punch (4-HP) and (b) six-hole punch (6-HP)

Table 3.1: Validation coupon critical dimensions

Dimension	Measurement (mm)
W	25.4
L	50.8
D1	7.938
D2	3.967
t	2.0

3.2.2 Mechanical testing

The test matrix in Table 3.2 summarizes the full experimental program to characterize Viton RB75A5, in which a minimum of three tests were performed for each test type (quantity of tests performed is indicated by the numbers in the table). The material was tested at multiple strain rates to evaluate strain-rate dependency in uniaxial tension (UT) and uniaxial compression (UC). Cyclic loading/unloading was performed to evaluate the significance of viscoelastic hysteresis and/or the Mullins softening effect. Creep testing was done to further quantify viscoelastic effects. High-temperature tests were performed to explore temperature sensitivity. Finally, the material was tested in two additional stress states (pure shear (PS) and simple shear (SS)) to enhance the predictive fidelity of the constitutive models. Validation experiments involving tension coupons with through-holes (Figure 3.2) were performed to validate the predictive capabilities of the calibrated constitutive models under a complex, three-dimensional, multi-axial stress state (that differs from the simple stress states they were calibrated to).

Table 3.2: Material characterization test matrix

Test	UT	UC	PS	SS	Validation
Low Rate	3	3	-	-	-
Quasi-Static	3	3	3	3	-
High Rate	3	3	-	-	-
Cyclic/Mullins	3	3	-	-	-
Creep	3	-	-	-	-
HT (85, 140, 200 °C)	3	-	-	-	-
DIC	3	-	-	-	3

All quasi-static tension tests were conducted in accordance with the ASTM D412 test standard [32]. An Instron 3365 extended-height, screw-driven universal testing machine with pneumatic side-action tensile grips was used to load the specimens (Figure 3.3). The crosshead was actuated at 50 mm/min to ensure nearly quasi-static loading conditions. For all tension testing (strain rate, cyclic, creep), the load frame was equipped with a 2-kN load cell, and recorded engineering strain using a clip-on extensometer. The extensometer measures the length change ΔL during testing between two points in the gage section initially separated by a distance L_0 = 25.4 mm. The instantaneous length change ΔL is normalized by the characteristic length L_0 to provide the axial engineering strain $\epsilon_{eng} = \Delta L/L_0$. Within this length-averaged measurement is the deformation in the gage section (within the extensometer window), which is nearly homogeneous to fracture. The digital image correlation experimental results in Section 3.3.3 provide insight into the local strain at fracture, which cannot be captured with an extensometer.

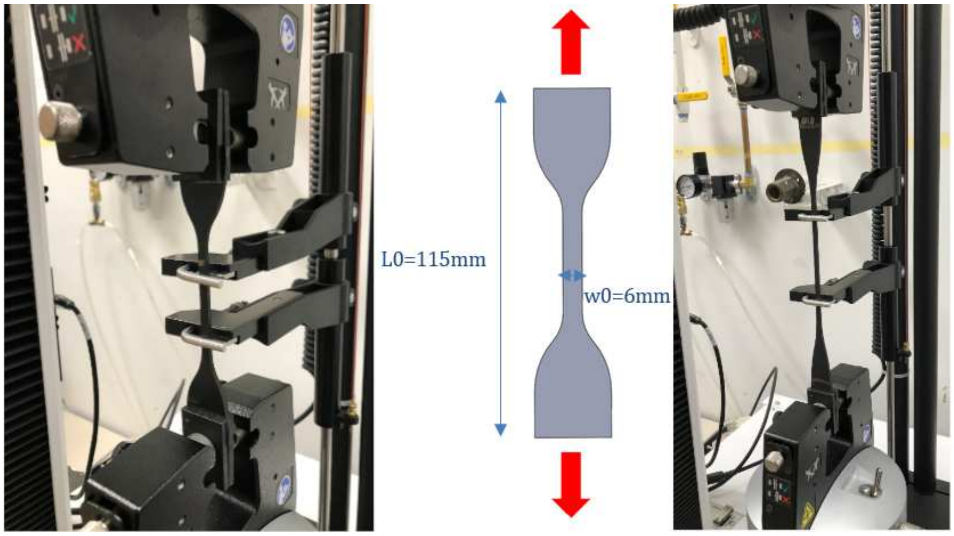

Figure 3.3: Uniaxial tension testing

Quasi-static compression tests were conducted in accordance with ASTM D575 [33] on an Instron 3365 universal testing machine under ambient conditions using custom compression platens. Tests were performed with the crosshead moving at a rate of 12.5 mm/min. For all compression testing (quasi-static, cyclic), the test machine was equipped with a 5-kN load cell for force measurement. Engineering strain was calculated using the crosshead displacement (measured by the built-in LVDT) divided by the original height of the test specimen. Engineering stress was calculated as force divided by the original cross-sectional area.

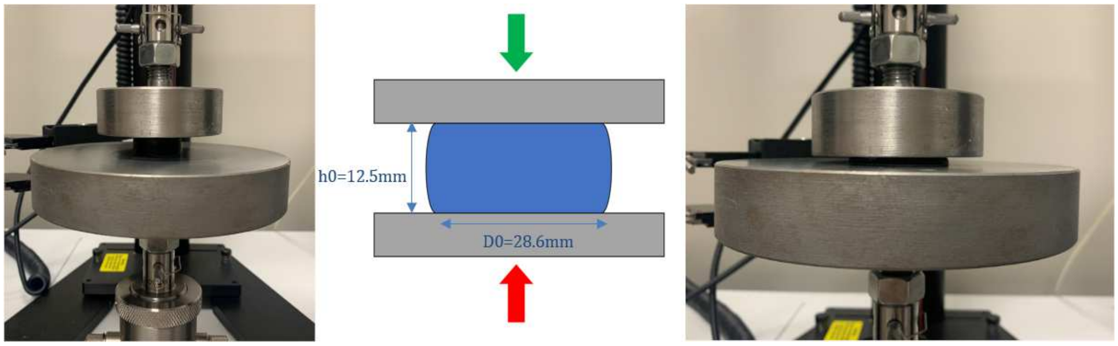

Figure 3.4: Uniaxial compression testing

To investigate strain-rate dependence, uniaxial tension and compression testing was performed at crosshead displacement rates of 5 and 500 mm/min, and compared to the quasi-static tests performed at 50 mm/min.

A set of tests involved loading/unloading to 80% strain three times, and heat cycling the sample (ramping up to and holding at 200 °C for 8 hr) before repeating the test. This test (three load/unloads) was repeated five times on the same sample. Another set of tests consisted of loading/unloading in uniaxial tension to 40% strain three times, heat cycling, loading/unloading to 80% strain three times, heat cycling again, and finally loading/unloading to 120% strain three times, all on the same sample. In addition, samples were tested in cyclic compression by loading to an engineering strain of 32% and unloading to a resultant force of 0.1 kN.

Creep testing was performed, and was initialized by 50 mm/min displacement control until a load of 48.5 N was reached (approximately 50% of the UTS). The test proceeded under force control, holding the applied load fixed at 48.5 N for greater than 19 hrs and measuring the resulting evolution of displacement with time.

Viton RB75A5 was also tested in uniaxial tension at elevated temperatures to understand the impact of real-time, in situ temperature effects on mechanical behavior (in contrast to thermal conditioning, i.e., thermally cycling/aging prior to mechanical testing). High-temperature uniaxial tension tests were conducted using an Instron 68TM axial load frame system (Model 2525-818) equipped with an environmental chamber and mechanical wedge action tensile grips. A 2-kN load cell was used for force measurement, and strain was measured using an AVE2 2663-902 video extensometer equipped with a 9 mm lens. Tests were performed at controlled temperatures of 85, 140, and 200 °C. The loading rate was 50 mm/min, with each sample soaked at its respective testing temperature for 10 minutes prior to testing.

Pure shear testing was performed following methods similar to Meunier [7]. The $150 \times 70 \times 2$ mm specimen 3.1d was gripped using a custom mechanical fixture (26 mm on each end of its 70 mm width; Figure 3.5). The specimen was actuated under displacement control at a constant crosshead speed of 50 mm/min. Engineering strain was calculated optically, tracking the displacement of two marked dots using ImageJ, and dividing by the original distance between the two marked dots (5 mm). Engineering stress was calculated as force (measured by a 5-kN load cell) divided by the original cross-sectional area (nominally 150 mm wide and 2 mm thick).

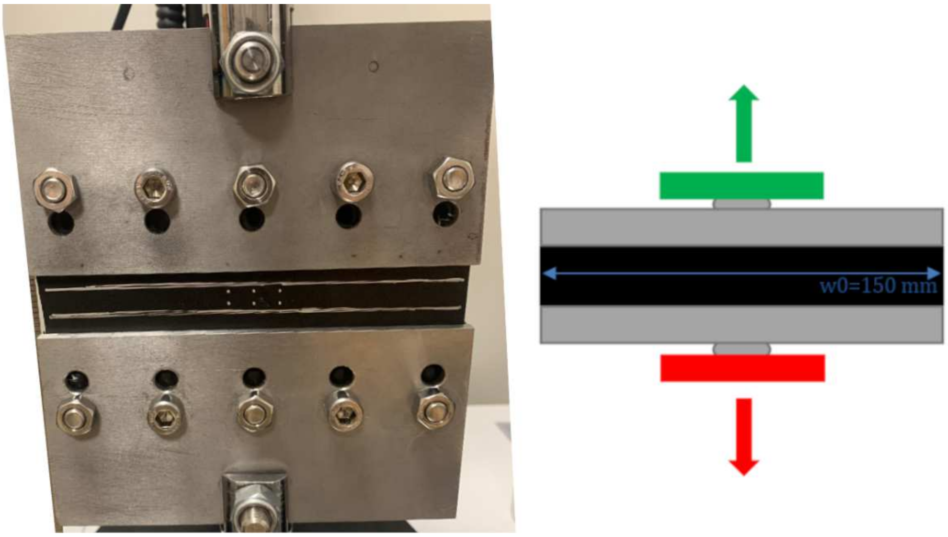

Figure 3.5: Pure shear testing

Simple shear testing was conducted following methods similar to the ASTM D1002 test standard (Standard Test Method for Apparent Shear Strength of Single-Lap-Joint Adhesively Bonded Metal Specimens by Tension Loading) [34]. The Instron universal testing machine was equipped with a 2-kN load cell for force measurement. Multiple adhesives were evaluated (pel-seal, VHB adhesive, structural caulk sealant, and various double-sided tapes), but only an epoxy structural adhesive (McMaster-Carr, item 7524A14) worked well in obtaining meaningful simple shear deformation of the specimen prior to delamination from the laps. The epoxy was applied to each face of the specimen, and the specimen was bonded to aluminum or stainless steel laps, resting flat for 72 hr at room temperature with no external pressure, as recommended by the manufacturer. PLA shims were FDM 3D printed to function as “spacers” to align the load train. Spacers were printed individually to account for specimen thickness differences to ensure each test was properly aligned, as seen in Figure 3.6. Tests were conducted at a crosshead displacement rate of 50 mm/min. Strain was calculated using the crosshead displacement of the load frame (measured by a built-in LVDT) divided by the specimen thickness, and stress was calculated using the force divided by the cross-sectional area of the binding face of the specimen. Too thin epoxy application led to debonding, where the specimen slid off the lap without significant internal deformation. Epoxy applied too thick led to obstructed motion of the frame, which impacted the sample's deformation. After several iterations, three proper tests with optimal epoxy application and limited test obstruction were obtained.

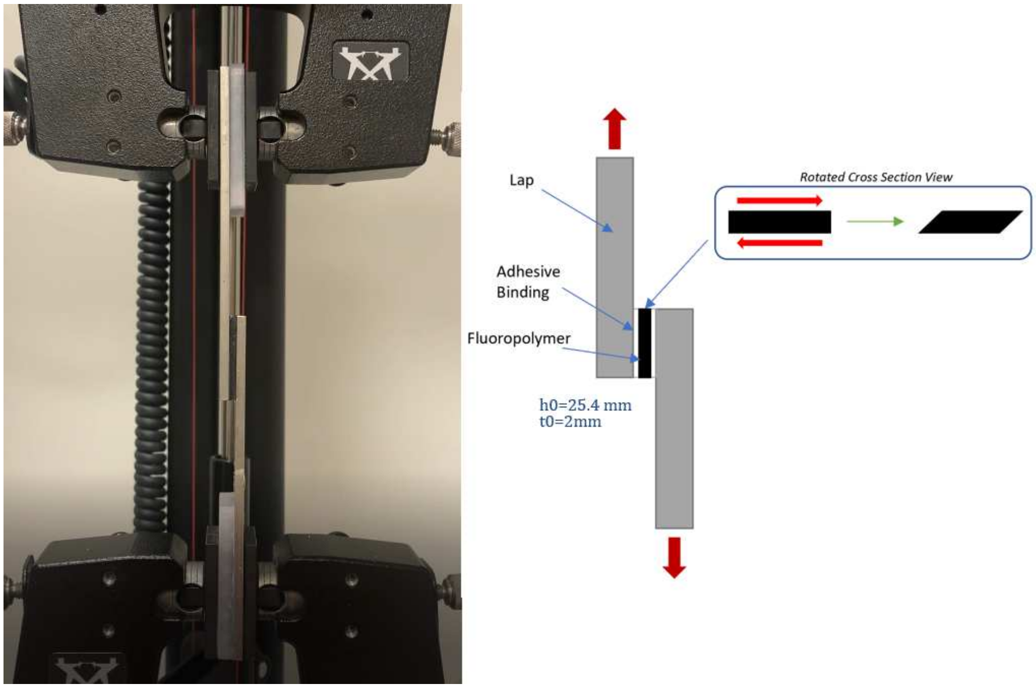

Figure 3.6: Simple shear testing

Quasi-static DIC tensile tests and validation tests were performed under displacement control to get localized principal strain data in real-time and full-field deformation contours. Testing was done with a constant speed of 50 mm/min to match the same conditions used to calibrate the constitutive model and to ensure quasi-static conditions. An Instron 3365 extended-height, screw-driven universal testing machine with pneumatic side-action tensile grips was used to load the specimens. A 2-kN load cell was used to detect force, and displacement was measured by the LVTD. The Good Practices Guide for Digital Image Correlation was consulted for experimental methods [35].

3.2.3 Digital image correlation

A high-contrast (white) speckle pattern was applied to all specimens using a gravity-fed airbrush (G222 Pro Set, Master Airbrush) and white paint. Examples of speckled tension and validation samples are displayed in Figures 3.7 and 3.8.

Figure 3.7: High-contrast speckle pattern applied to a tension specimen

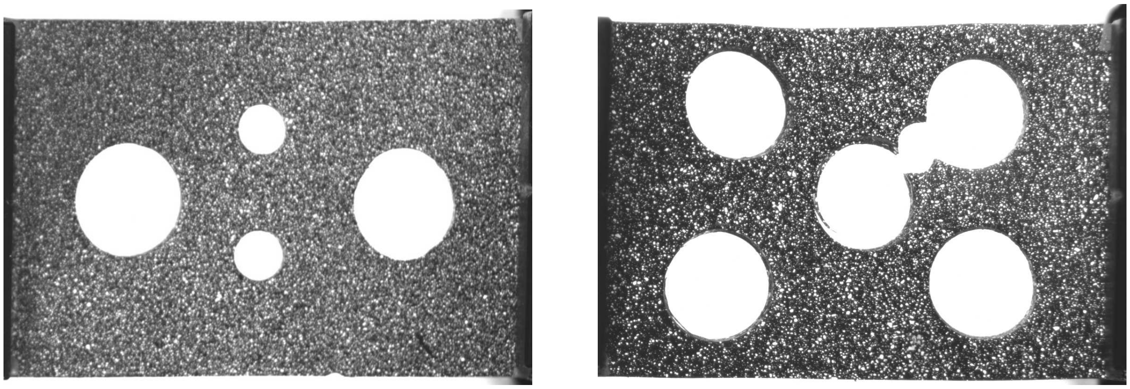
(a)
(b)

Figure 3.8: High-contrast speckle pattern applied to (a) four-hole and (b) six-hole validation specimens

A 2D camera setup with a high-performance machine vision camera (Blackfly USB3, FLIR) and a 35-mm focal length lens (HP series, Edmund Optics) was used to capture images during testing. The resulting images were processed using commercial DIC software (VIC-2D, Correlated Solutions). References [35] and [36] were followed for post-processing procedures. A Gaussian low-pass logarithmic filter was applied during correlation, which averages the strain value at each pixel to reduce noise and present a clear and uniform strain measurement. For the tension testing, incremental correlation was used to achieve correlation to fracture. The incremental correlation was not necessary for validation testing. A virtual extensometer (VE) and virtual strain gauge (VSG) were used to track the principal strain at selected "hot spots" in the tension and validation coupons where strain localizations emerged during the tests. The VSG size reported in Tables 3.4 and 3.3 is calculated using Eq. (3.1) below (from reference [35]), then converted from pixels to mm using the image scale (in mm/pixel).

$$L_{VSG} = (L_{window} - 1)L_{step} + L_{subset} \tag{3.1}$$

The DIC setup and processing parameters for tension and validation testing are summarized in Table 3.3 and Table 3.4:

Table 3.3: DIC settings – tension tests

Test	Subset	Step	Filter Size	mm/pixel	VSG Size (pixels)	VSG Size (mm)
R3-3	19	3	5	0.0750	31	2.326
R3-4	17	2	5	0.0751	25	1.877
R4-1	15	2	5	0.0809	23	1.862

Table 3.4: DIC settings – validation tests

Test	Subset	Step	Filter Size	mm/pixel	VSG Size (pixels)	VSG Size (mm)
4-HP	23	2	5	0.0339	31	1.052
6-HP1	29	2	15	0.0332	57	1.894
6-HP2	19	3	5	0.0337	31	1.046
6-HP3	25	1	5	.0331	29	0.950

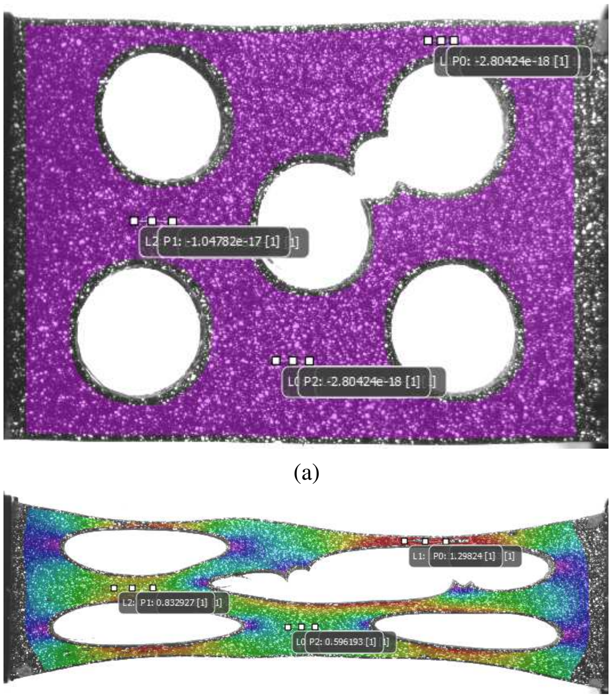

(a)

(b)

Figure 3.9: Virtual strain gage (VSG) locations (a) in undeformed coupon and (b) in deformed coupon just prior to fracture

3.3 Experimental Results

3.3.1 Viscoelasticity and Mullins effect

Figure 3.10 shows the response of Viton RB75A5 in uniaxial tension and uniaxial compression at three different loading rates (5, 50, and 500 mm/min). The material shows weak rate dependence in tension and only modest rate dependence in compression, suggesting that neglecting viscoelastic physics in the constitutive model is likely reasonable for many practical applications. A 50 mm/min loading rate was used throughout the rest of the tests. It is worth noting that the uncured RB75A5 is significantly softer than the post-cured material previously tested (refer to Chapter 2), as the post-cure fundamentally alters the material chemistry (facilitates cross-linking), leading to a stiffer stress-strain response.

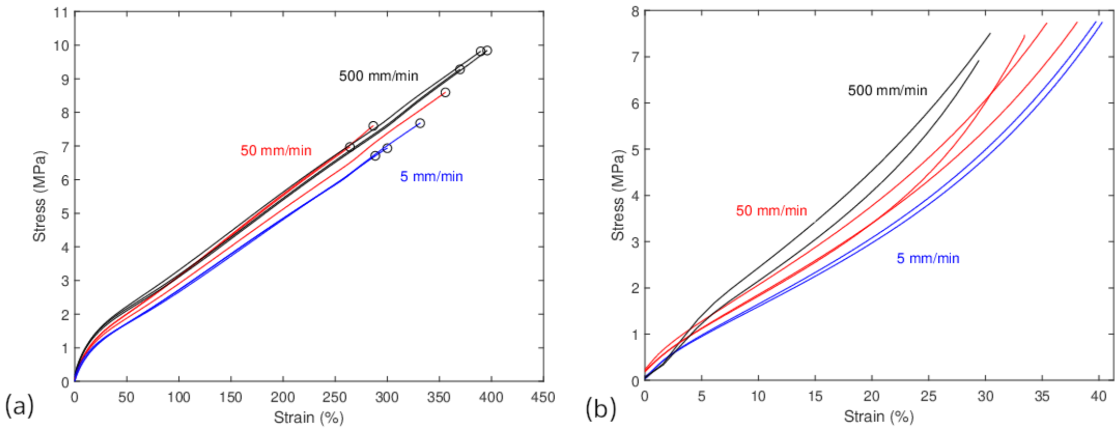

Figure 3.10: Variable strain rate testing in (a) uniaxial tension and (b) uniaxial compression

Figure 3.11 displays the response of a single sample that was tested in cyclic tension to 80% strain. Each test consisted of an initial loading (labeled “initial stretch”), unloading, and then subsequent loading twice more (labeled “secondary stretches”). This process was repeated five times with the same sample. Between each test, the sample was thermally aged by ramping to 200 °C, holding at isothermal conditions for 8 hr, and ramping down to room temperature. The material was weakly viscoelastic (indicated by the modest hysteresis loops), with an essentially negligible permanent set. The unloading curves in Figure 3.11 show the material does not elastically relax at the same rate that it is unloaded during testing. In addition, there is a Mullins softening effect: if the material is repeatedly stretched, the initial stretch is notably stiffer than subsequent (secondary) stretches. The cross-linking due to thermal aging tends to compete with the Mullins softening effect, as the initial stretch on the same sample nearly returned to its initial stiffer state for Tests 2-5. These results are important to consider in the desired sealant application, as the material will often be repeatedly deformed while being exposed to extreme thermal conditions.

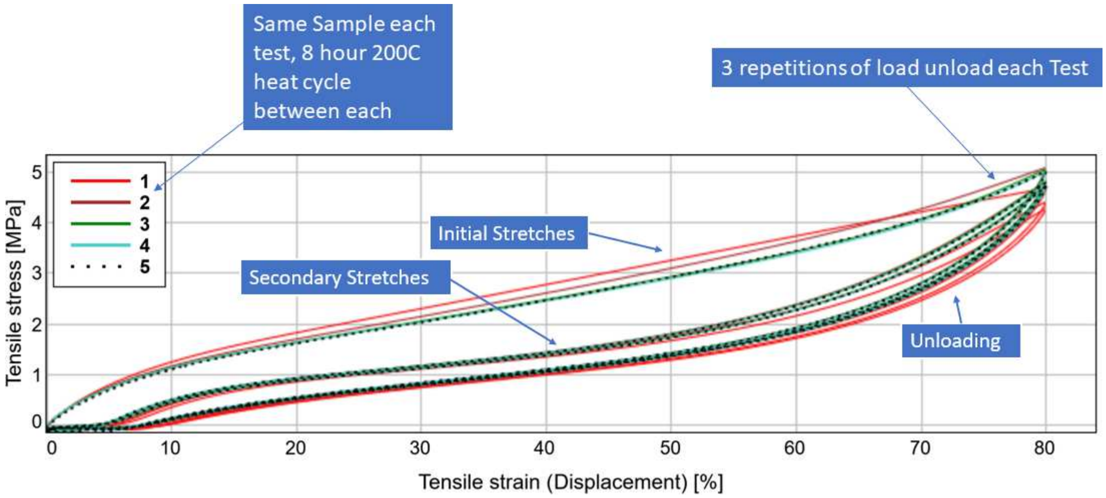

Figure 3.11: Cyclic tension to 80% strain, with thermal aging between cycles

Figure 3.12 displays the response of a single sample tested in cyclic tension three times (three cycles each time). The sample is thermally aged between tests (ramp to 200 °C and hold for 8 hr.), and the elongation is increased with each subsequent test. These results demonstrate the significance of the Mullins softening effect at varying levels of elongation, where there is a greater effect at higher elongations. The softening effect is only apparent, however, prior to heat-cycling. For instance, Test 2 was performed after the sample was cycled three times to 40% strain (during Test 1); in its first cycle to 80% strain (during Test 2), the material response returned to its original path in the 40-80% elongation window. Test 3 exhibits the same response, with a softened stress-strain response up to 80% strain, and then returns to its original path from 80-120% strain.

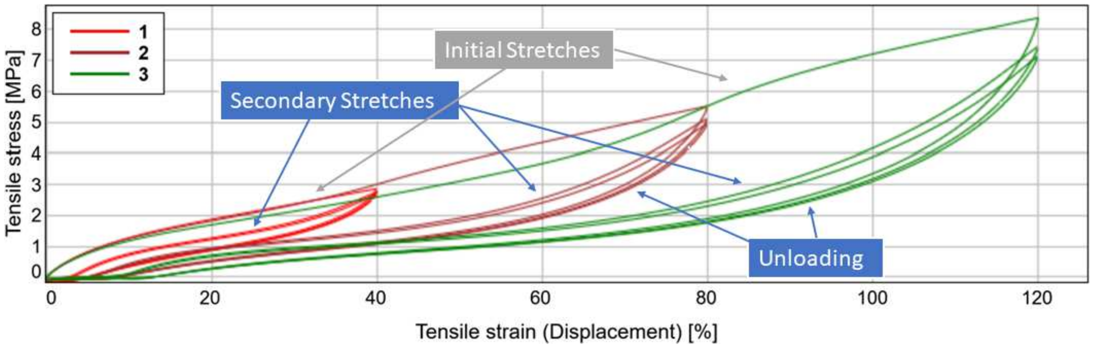

Figure 3.12: Cyclic tension to 40%, 80%, and 120% strain (three cycles each), with thermal aging between stretch increases

Figure 3.13 displays a creep test. In each of the three tests, the material reached 350% strain within seconds and 400% strain within several hours. The strain only increases modestly over tens of hours, suggesting that this material is only weakly viscoelastic, consistent with the results of the strain rate series and cyclic series. As a result, viscoelastic physics was withheld from our constitutive modeling in the present work.

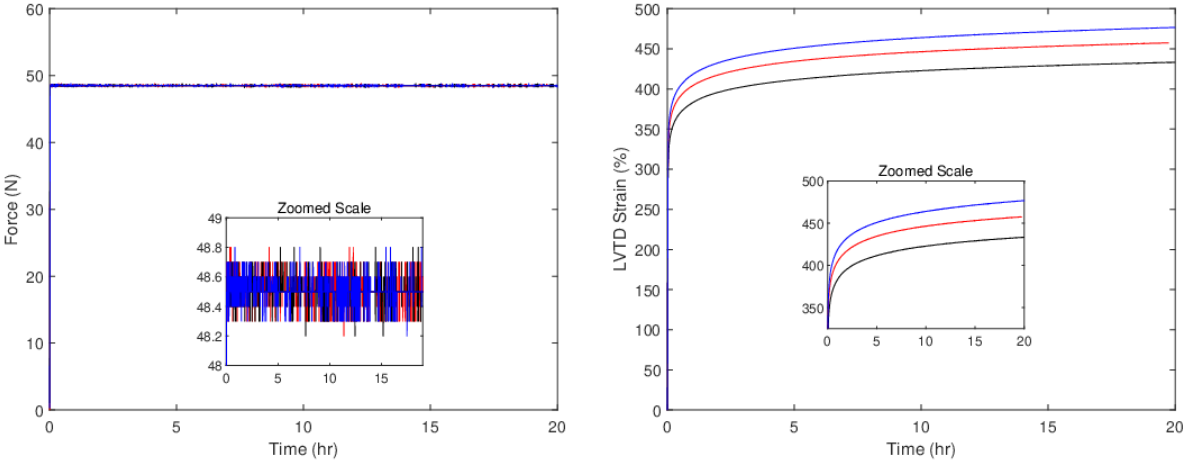

Figure 3.13: Creep test: (a) step increase in force (controlled) and (b) time-dependent strain response (measured)

Figure 3.14 displays a cyclic compression test with three load-unload cycles to a maximum displacement of 4 mm and a minimum force of 0.1 kN. Three tests were performed and showed good repeatability, but for ease of visualization, only one test is shown here. A prominent Mullins effect signature is visible, indicated by the softened response during the second loading cycle. The material was weakly viscoelastic (indicated by the modest hysteresis loops), with an essentially negligible permanent set.

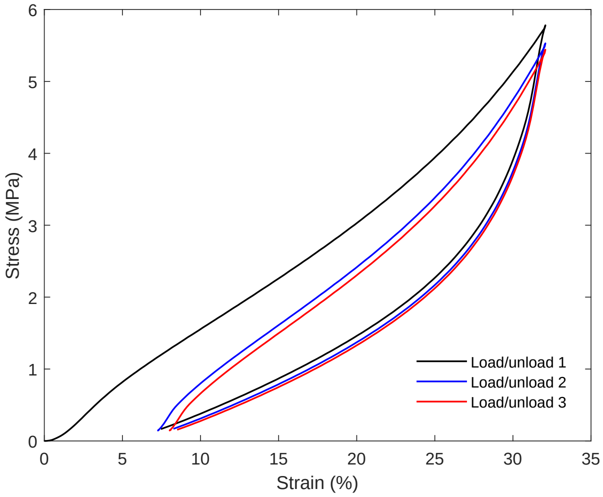

Figure 3.14: Cyclic compression stress-strain response

3.3.2 High-temperature response

Viton RB75A5 was also tested at elevated temperatures of 85, 140, and 200 °C (Figure 3.15). As expected, higher temperatures led to softer behavior and earlier fractures. The tests at 85 °C resulted in an average UTS of 3.9 MPa, with an elongation of 133% and a one-percent modulus of 9.6 MPa. The 140 °C tests resulted in an average UTS of 2.5 MPa, with an elongation of 73.6% and a one-percent modulus of 7.6 MPa. The 200 °C tests resulted in an average UTS of 1.9 MPa, with an elongation of 48.6% and a one-percent modulus of 4.7 MPa. Higher temperatures softened the material behavior (lower modulus) and resulted in fracture at lower elongations (and thus lower ultimate tensile stresses).

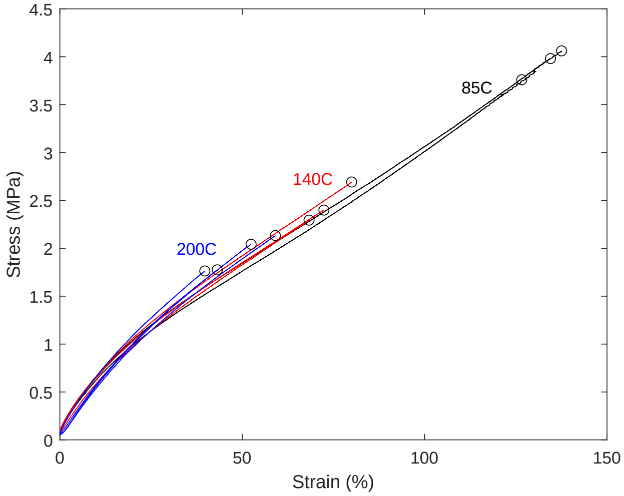

Figure 3.15: Uniaxial tension tests at elevated temperatures: 85, 140, 200 °C

3.3.3 Quasi-static response

Quasi-static tension and compression results are embedded in Figure 3.10, wherein the 50 mm/min tests were used for quasi-static analysis.

Figure 3.16 displays the frame prior to fracture for a tensile test with DIC. This provides insight as to the principal strain for homogeneous deformation of the RB75A5 in tension but is not necessary for the model calibration because quasi-static tests were done with an extensometer and the models were calibrated using engineering strain as inputs. 3.3 and Table 3.4. Figure 3.17 displays the principal strain measured from virtual strain gauges both in the middle and point of fracture of the tensile specimen. The “middle” label within the legend describes placement in the middle of the specimen, while the “fracture” was the VSG placed at the point of fracture. The three tests resulted

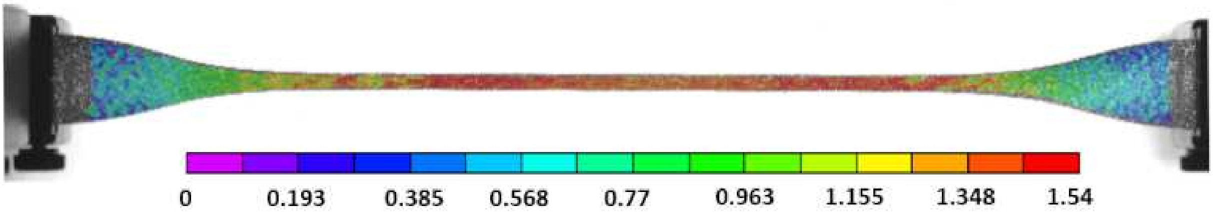

Figure 3.16: Maximum principal strain contour from a tensile test with DIC

in a successful correlation to fracture, fracturing at a maximum principal strain of 1.40 mm/mm (140%) on average.

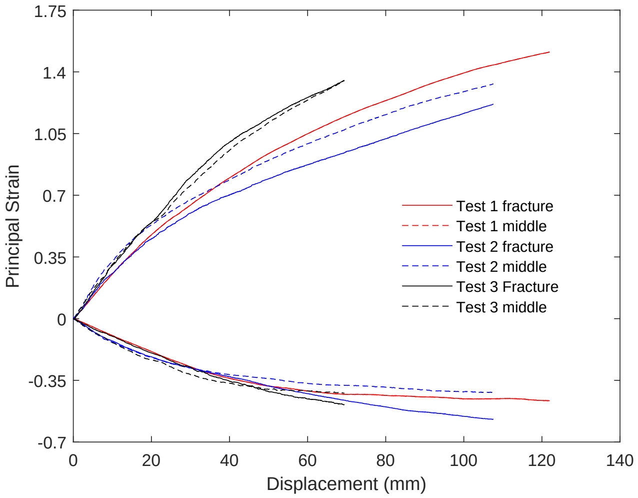

Figure 3.17: Tension DIC Results

Pure shear testing was done to give insight into how the material behaves in a non-uniaxial stress state. Figure 3.18a shows the discrete, raw data obtained from testing, which exhibited some noise. Because the stress-strain curve needs to start at (0,0) for constitutive model calibration, the raw data was zeroed. To reduce the noise, a built-in curve fitting/interpolation subroutine in Matlab was used to smooth the discrete, raw stress-strain data (Figure 3.18b). Test 3 was the only test to fracture in-test (at the grip), with an elongation of 81% and UTS of 3.2 MPa.

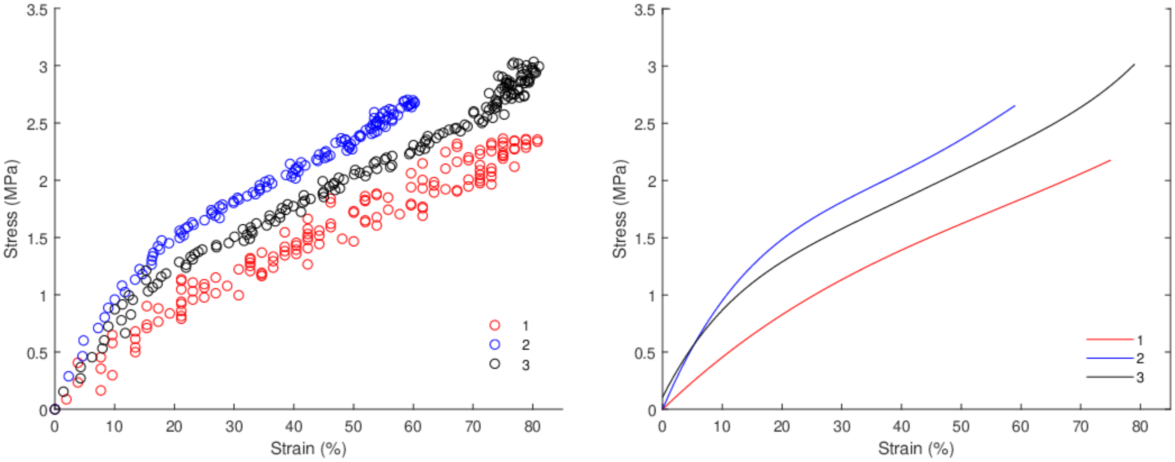

Figure 3.18: Pure shear (a) discrete raw data and (b) smoothed data

Simple (lap) shear testing results are displayed in Figure 3.19. It is worth noting that the tests terminated due to adhesive failure, indicating the shear fracture strength of the material is larger than the bond strength at the material-lap interface. Up to adhesive failure, however, the samples underwent simple shear deformation (i.e., changed shape from a rectangle into a parallelogram).

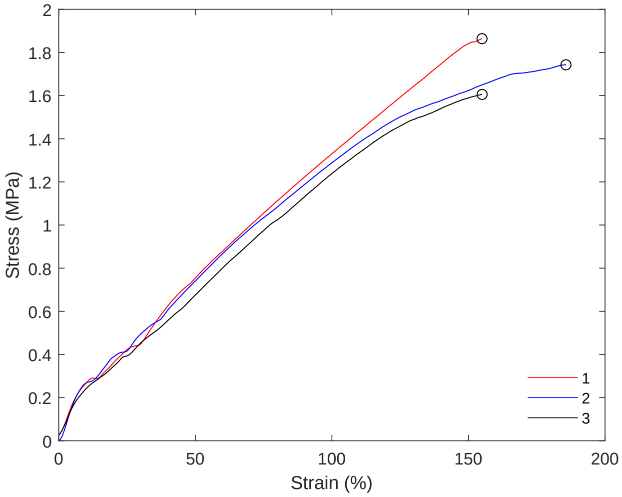

Figure 3.19: Results from lap shear testing

3.4 Constitutive Model Calibration

In this section, two popular parameterized hyper-elastic constitutive models, Mooney-Rivlin and Ogden, were calibrated. In addition, one tabulated model was used (MAT_181 in LS-DYNA's hyper-elastic material library).

The stress-stretch relation in uniaxial tension for the Mooney-Rivlin model is displayed in Eq. (3.2) below, where T_0 is the engineering stress, λ is the stretch, and c_1 and c_2 are the optimized, material-specific parameters:

$$(\mathrm{T}_0) = 2\left(\lambda - \lambda^{-2}\right)\left(\mathrm{c}_1 + \lambda^{-2}\mathrm{c}_2\right) \tag{3.2}$$

The stress-stretch relation in uniaxial tension and uniaxial compression for the Ogden model is displayed in Eq. (3.3) below:

$$(\mathrm{T}_0) = \mu_1\left(\lambda^{\alpha_1 - 1} - \lambda^{-\frac{1}{2}\alpha_1 - 1}\right) + \mu_2\left(\lambda^{\alpha_2 - 1} - \lambda^{-\frac{1}{2}\alpha_2 - 1}\right) + \mu_3\left(\lambda^{\alpha_3 - 1} - \lambda^{-\frac{1}{2}\alpha_3 - 1}\right) \tag{3.3}$$

where α_1, α_2, α_3, μ_1, μ_2, and μ_3 are material-specific constants to be calibrated to the test data. The pure shear Ogden constitutive equation is displayed in Eq. (3.4) below:

$$(\mathrm{T}_0) = \mu_1 \left(\lambda^{\alpha_1 - 1} - \lambda^{-\alpha_1 - 1}\right) + \mu_2 \left(\lambda^{\alpha_2 - 1} - \lambda^{-\alpha_2 - 1}\right) + \mu_3 \left(\lambda^{\alpha_3 - 1} - \lambda^{-\alpha_3 - 1}\right) \tag{3.4}$$

The poly-convexity constraint, ensuring the energy function is convex with respect to the deformation gradient tensor and its spatial gradient, is enforced through the requirement:

$$\mu_k \times \alpha_k > 0 \tag{3.5}$$

where k=[1, 2, 3].

Non-least squares optimization (NLS) techniques were used for the development of constitutive models. This optimization program finds the global minimum error for model-to-data comparison. The mathematical constants determined from the curve-fitting program were imported directly into LS-DYNA to incorporate the hyper-elastic models. The tabulated MAT181 involved a direct compressive and tensile engineering strain-stress curve import into LS-DYNA.

Mooney-Rivlin incorporates only tension testing, and Ogden incorporates additional stress states. Only tests to failure were used in calibration, so the simple shear tests were excluded. In the validation, the following varieties of curves were used for Ogden: uniaxial tension only (UT), uniaxial tension and uniaxial compression (UT+UC), and the combination of uniaxial tension, uniaxial compression, and pure shear (UT+UC+PS). Figure 3.20 displays the NLS curve fitting on tension, compression, and pure shear with the Ogden constitutive equation.

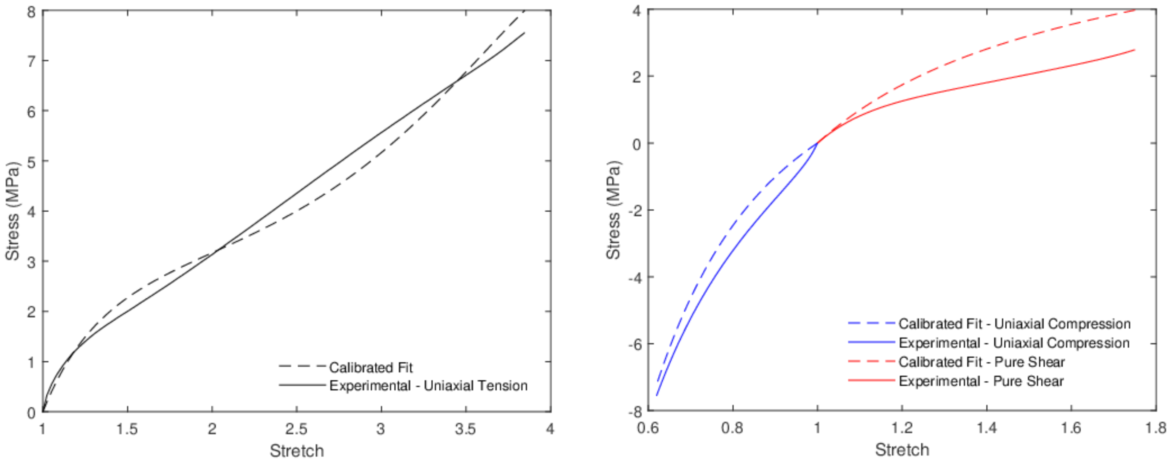

Figure 3.20: Ogden hyper-elastic constitutive model calibration: (a) uniaxial tension, (b) uniaxial compression and pure shear

A similar process was used for all other constitutive models. Table 3.5 displays the rounded constants utilized in each material card. For Ogden, c1, c2, and c3 represent the μ variables, and c4, c5, and c6 represent the α variables.

Table 3.5: Hyper-elastic constitutive model constants

Constants						
Constitutive Equation	c1	c2	c3	c4	c5	c6
Mooney-Rivlin	1.376	2.757	-	-	-	-
Ogden (UT)	1.33E-5	23.034	1.06E-12	3.557	0.309	5.102
Ogden (UT+UC)	0.0562	0.0561	-6.331	3.858	3.858	-0.923
Ogden (UT+UC+PS)	-1.53E-8	-7.125	0.0575	14.013	-0.761	4.474

The MAT181 tabulated constitutive model was calibrated directly within LS-Prepost. The tensile and compressive data were combined into a singular load curve with negative compressive stress-strain data and positive tensile stress-strain data, passing through the origin at (0,0). To aid the simulation time and performance, the number of data points was downsampled from 19557 to 125 seen in Figure 3.21 below:

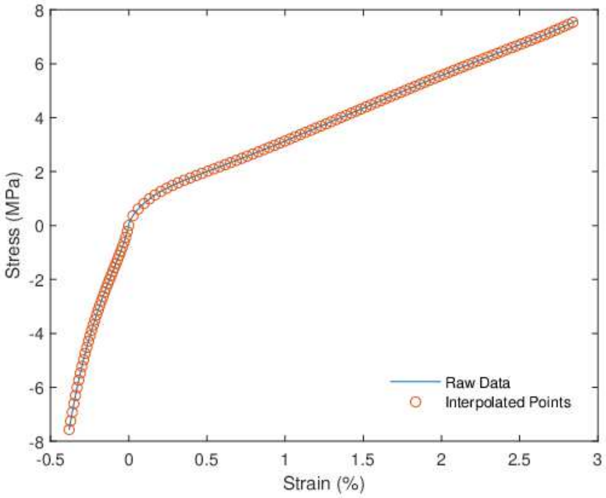

Figure 3.21: Interpolated Compressive and Tensile Curves for MAT181 Material Card Import

3.5 Finite Element Analysis

3.5.1 Pre-processing: 3D solid modeling and meshing

For finite-element analysis (FEA) pre-processing, 3D CAD models of the validation coupons were created in SolidWorks (Dassault Systemes, 2023 Student Edition). It is important to model each test specimen using its exact dimensions (not the nominal dimensions in Figures 3.1 and 3.2) to best match the simulation to its respective test. Each 3D solid model was then imported into HyperMesh (HyperWorks, v. 2022, Altair, Troy, MI) for finite element meshing. The mesh size selected was 0.2 mm, determined through a mesh convergence study. The meshed models contained 291,310 and 225,730 elements for the four-hole and six-hole coupons, respectively. A representative mesh for each of the validation tests is shown in Figures 3.22 and 3.23:

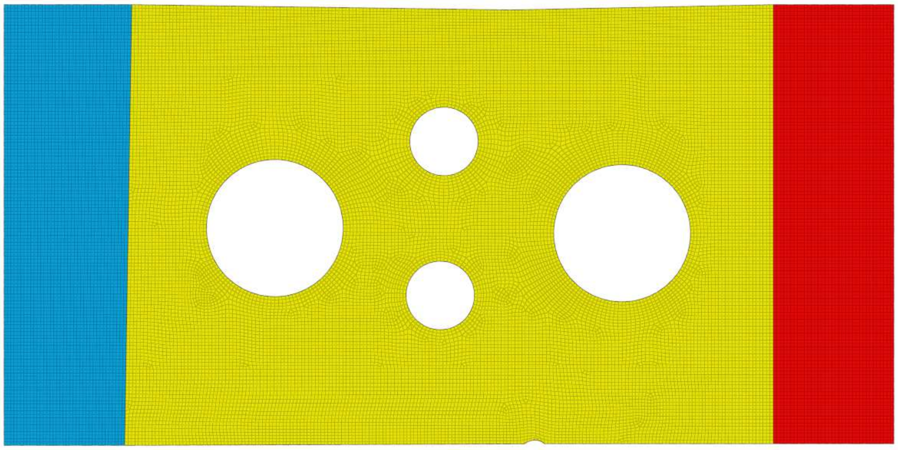

Figure 3.22: Representative mesh for four-hole validation coupon

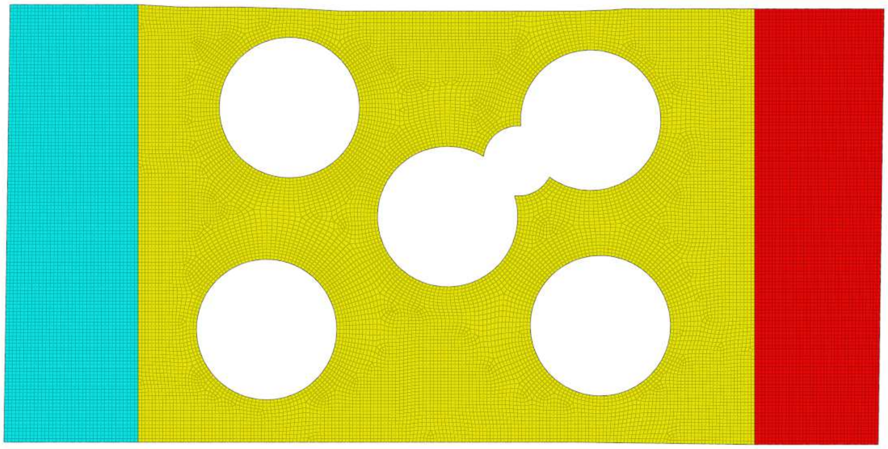

Figure 3.23: Representative mesh for six-hole validation coupon

3.5.2 Finite element simulations and post-processing

Numerical simulations were performed using an explicit solver in the commercial finite-element code LS-DYNA® (version R12.1.0, Ansys/LST, Livermore, CA). Three-dimensional, constant-stress 8-node solid hex elements (ELFORM=1) were used in the simulations. Stiffness-based hourglass control (IHQ=4) was employed with an hourglass coefficient QH=0.1 to account for the tendency of under-integrated elements to hourglass. Hourglass energies imposed by the hourglass control algorithm were found to be acceptably low in all simulations.

The specimen grip sections (denoted by blue and red shading in Figure 3.22 and Figure 3.23) were modeled as measured in the experiment (7 mm). One of the grip sections was held fixed (with all translational and rotational degrees of freedom constrained), while the other was prescribed an "artificial" constant velocity of 8.3 m/s. This "artificial" actuation speed is sufficiently high to meaningfully reduce the computational cost of explicitly simulating a quasi-static test, but sufficiently low to not introduce inertial effects, often observed as transient oscillations in material response (e.g., force vs. displacement) near simulation startup. Checking that the kinetic energy is an insignificant ratio of the internal energy also ensures minimized dynamic effects. A rigid material model (MAT_020) was assigned to both grip sections. The motion of the rigid gripped sections of the specimen was restricted using a center of mass constraint (CMO = 1) in MAT_020. For the fixed grip section, the constraint parameters were set to CON1 = CON2 = 7 to constrain all translational and rotational degrees of freedom. The gripped section driven by the uniaxial actuator was constrained using CON1 = 5, and CON2 = 7 so that only axial translation was permitted. The ungripped section of the specimen was modeled using the variety of constitutive models discussed in Section 3.4 (MAT_027 Mooney-Rivlin, MAT_077, MAT_181). For all material models, a density of 1.21E-9 tonne/mm^3, a modulus of 12.4 MPa (from average experimental values), and a Poisson's ratio of 0.495 weres used. Running in shared-memory parallel on eight CPUs, the simulations took anywhere from 12 to 48 hours, depending on available computational availability. VSG data was analyzed by selecting FEA elements matching the location and size of the VSG from DIC and comparing force-displacement, longitudinal principal strain, and transverse principal strain. The force-displacement was pulled from FEA using the *DATABASE_SECFORC card, and the displacement was tracked from the nodal displacement of the rigid grip. This force-displacement was compared to that of the Instron.

3.6 Constitutive Model Validation

For constitutive model validation, inhomogeneous coupon tests were performed to create a complex, three-dimensional, multi-axial deformation that differed from those the model had been calibrated to. Two validation tests were used: one with a 4-hole punch pattern (4-HP) and one with a 6-hole punch pattern (6-HP), as shown in Figure 3.8. One representative test for each coupon type was numerically simulated using FEA (see Section 3.5). FEA and DIC contour plots for maximum principal strain were compared at multiple different “global” strain levels, with the reported “global” strain as the crosshead displacement divided by the initial length of the coupon. To compare full-field strain measurement visually, the validation test’s maximum (longitudinal) principal strains (right) were compared to the finite-element simulations (left) at 25% strain increments. With the 4-HP validation test, there is visual and numerical validation up to 50% relative strain. For the 6-HP validation test, there is visual and numerical validation up to higher strains, extending to 120% relative strain.

Figure 3.24 shows a full field comparison at 25% strain. Overall, each constitutive model provides excellent replication of the validation test's longitudinal principal strain at early strain levels.

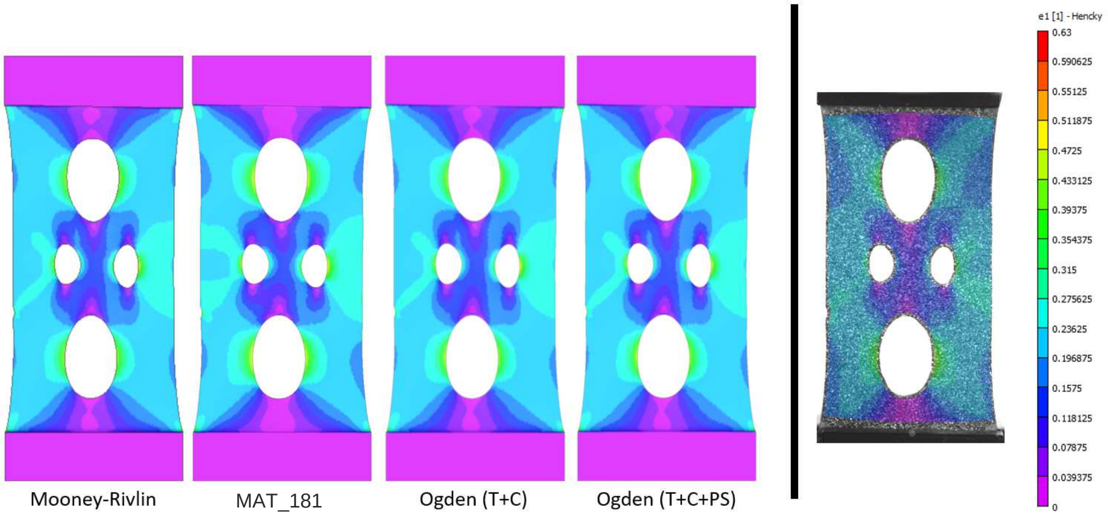

Figure 3.24: 4-HP 25% strain contour comparison

Figure 3.25 shows a full field comparison at 50% strain. Overall, each constitutive model provides a very good replication of the validation test (right) at this strain level. There are some differences in the area within the four holes, but overall the contour comparison matches extremely well.

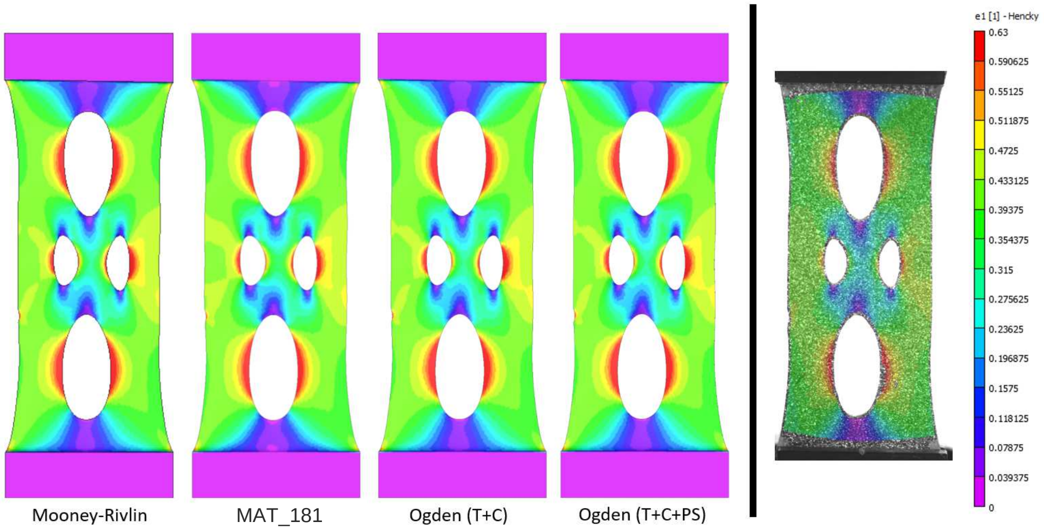

Figure 3.25: 4-HP 50% strain contour comparison

Force and principal strain histories were also used to benchmark the performance of the constitutive models. To accomplish this, virtual strain gauges (VSGs) were placed in three locations deemed as areas of interest (Figure 3.26). The displacements used in these history plots were correlated to the crosshead displacements in the experiment.

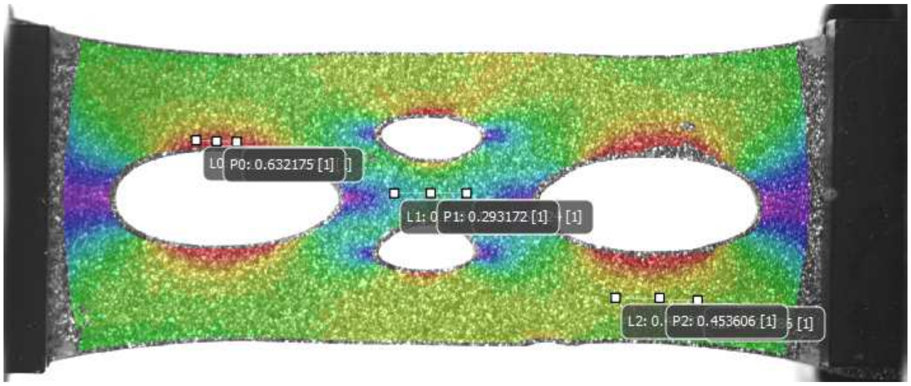

Figure 3.26: VSG locations in 4-HP (denoted “left,” “middle,” and “right”)

Figure 3.27 shows the “left VSG” from Figure 3.26. The longitudinal principal strain is captured well by all models at this level of strain. The transverse principal strain is captured well by all models, but it does not correlate quite as well as the longitudinal principal strain. For both the longitudinal and transverse strain, there is no visible difference between the “UTUC” and “UTUCPS” models, meaning the pure shear data does not add value to the Ogden model calibration at this early-strain level for replicating the experimental principal strains. The force-displacement curves were also compared, where the Mooney-Rivlin significantly overestimates the force response. Unlike before, the pure shear data adds value in accuracy when comparing the Ogden models. The MAT_181, however, is excellent in matching the force-displacement curve and is the best model at this level. Table 3.6 identifies numerical differences between the experiment and simulation through normalized root-mean-squared error (NRMSE). The Ogden and MAT_181 correlate very closely in the longitudinal direction, and the Ogden (UT+UC+PS) is the best numerically at the VSG location and up to the displayed strain level.

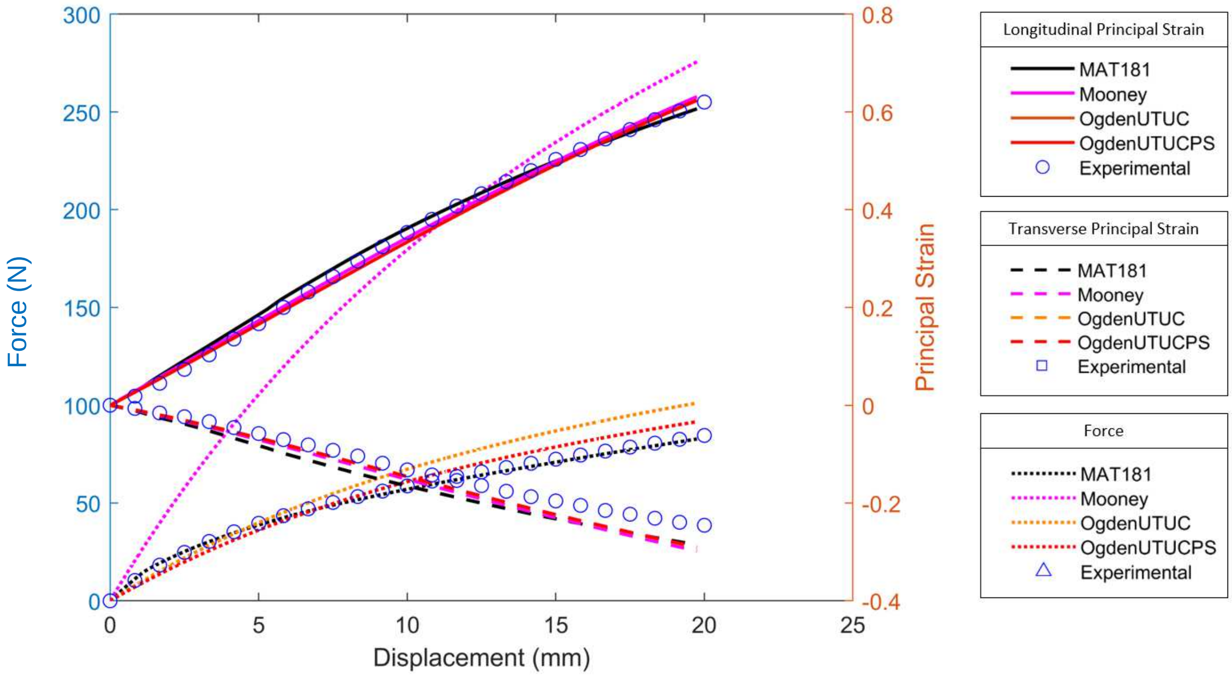

Figure 3.27: 4-HP validation (left VSG)

As anticipated from the contour comparisons, the maximum principal strain is not as well captured in the “middle VSG” results in Figure 3.28. The longitudinal and transverse principal strains, however, are captured reasonably well. The Ogden hyperelastic models coincide closely and match better than the MAT_181 in this location (Table 3.6). Note that the force-displacement shown here is the same as in Figure 3.27, which is independent of the VSG.

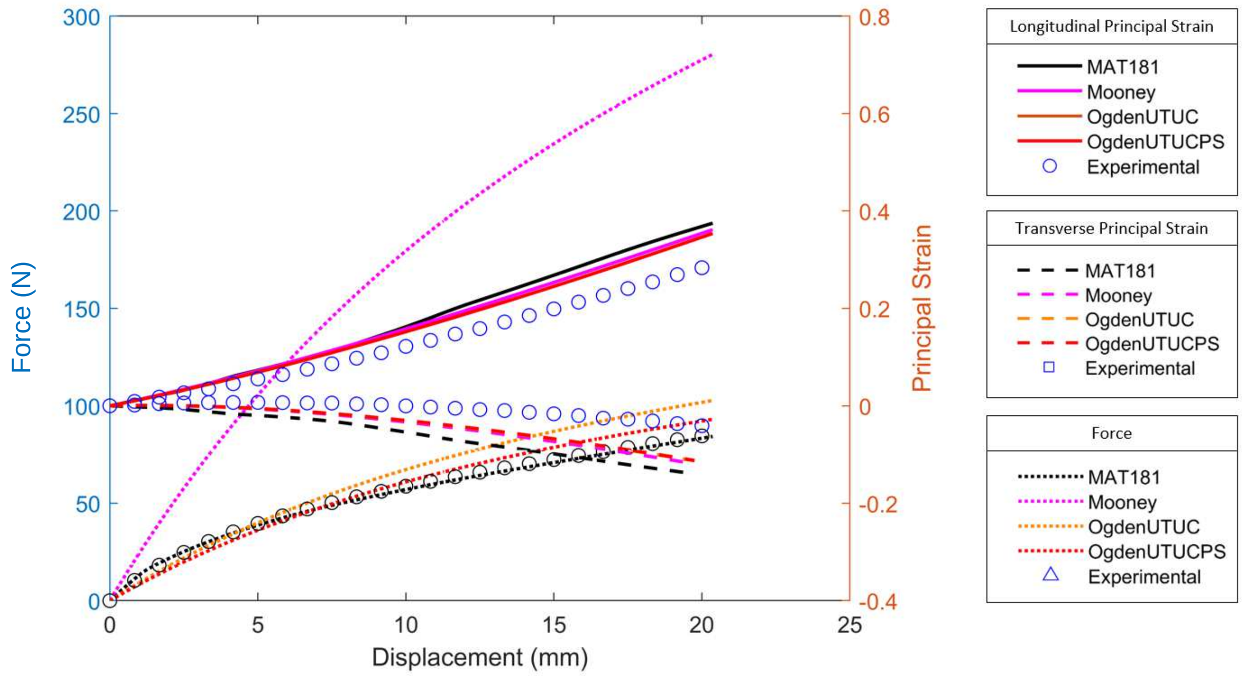

Figure 3.28: 4-HP validation (middle VSG)

Results from the "right VSG" plotted in Figure 3.29 show a close correlation between experiment and simulation, with minimal differences between constitutive models. Table 3.6 shows the Ogden constitutive models are the top performers, and there is minimal difference in adding the pure shear data when calibrating.

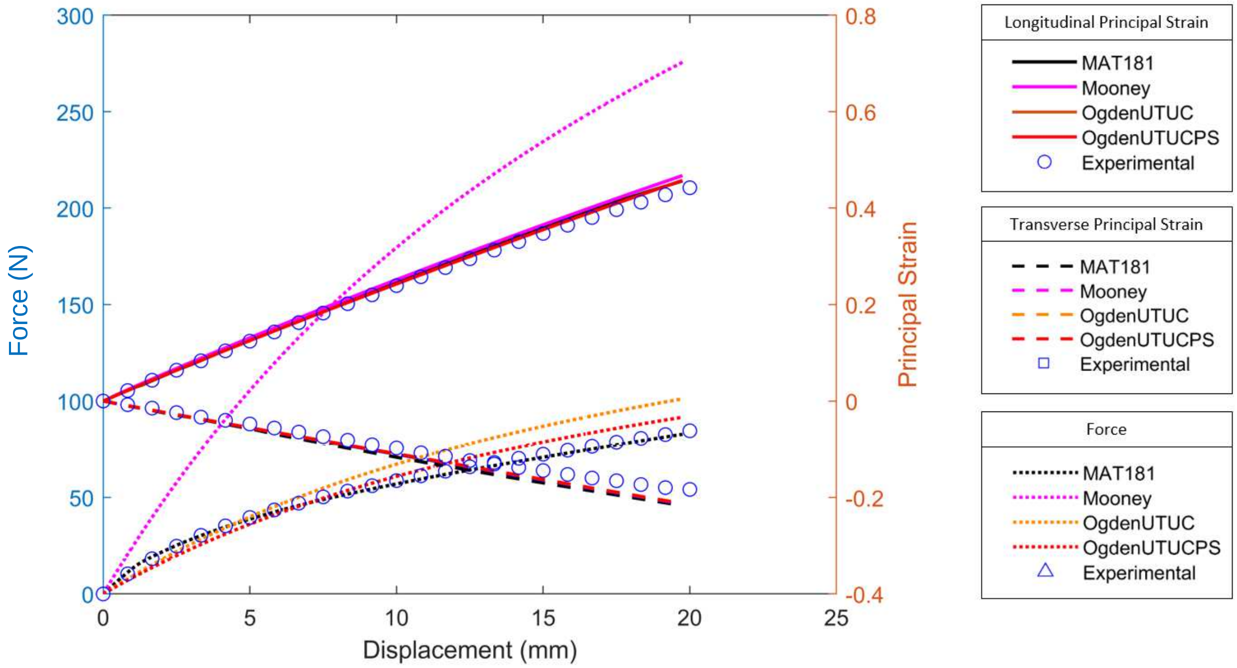

Figure 3.29: 4-HP validation (right VSG)

Table 3.6: 4-HP NRMSE

	MAT181	M-R	Ogden (UT+UC)	Ogden (UT+UC+PS)
Force	0.0155	0.4534	0.1028	0.0525
Left VSG				
Longitudinal	0.0189	0.0143	0.0184	0.0183
Transverse	0.1094	0.0940	0.0802	0.0793
Middle VSG				
Longitudinal	0.1386	0.1172	0.1030	0.1029
Transverse	0.4337	0.3534	0.3413	0.3398
Right VSG				
Longitudinal	0.0236	0.326	00176	0.0175
Transverse	0.0903	0.0737	0.0700	0.0693

To provide more proof of validation and to give more insight at higher strain levels, the 6-HP validation coupon is presented as well. The VSG for this validation coupon was placed at the location of maximum strain (and where fracture occurs). The DIC correlation carries nearly to fracture here (121% global strain), reaching 109% strain with complete correlation. Contour plot comparisons of the longitudinal principal strain are shown in 25% increments. Force-displacement comparison is also made in the VSG plot.

Figure 3.30 shows a full field longitudinal principal strain comparison at 25% global strain. Overall, each constitutive model provides excellent replication of the validation test at early strain levels.

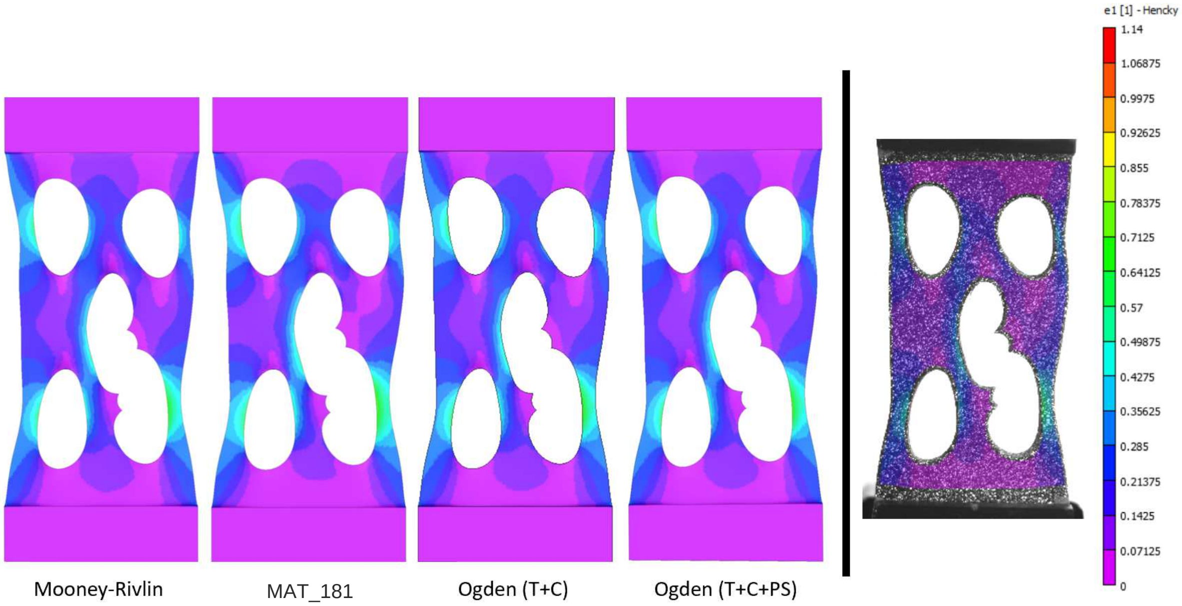

Figure 3.30: 6-HP 25% strain contour comparison

Overall, the Mooney-Rivlin, MAT_181, and Ogden models all capture the deformation well. We can see slight differences in Figure 3.31 in the circled area, where the Mooney-Rivlin and Ogden models over-predict the longitudinal principal strain.

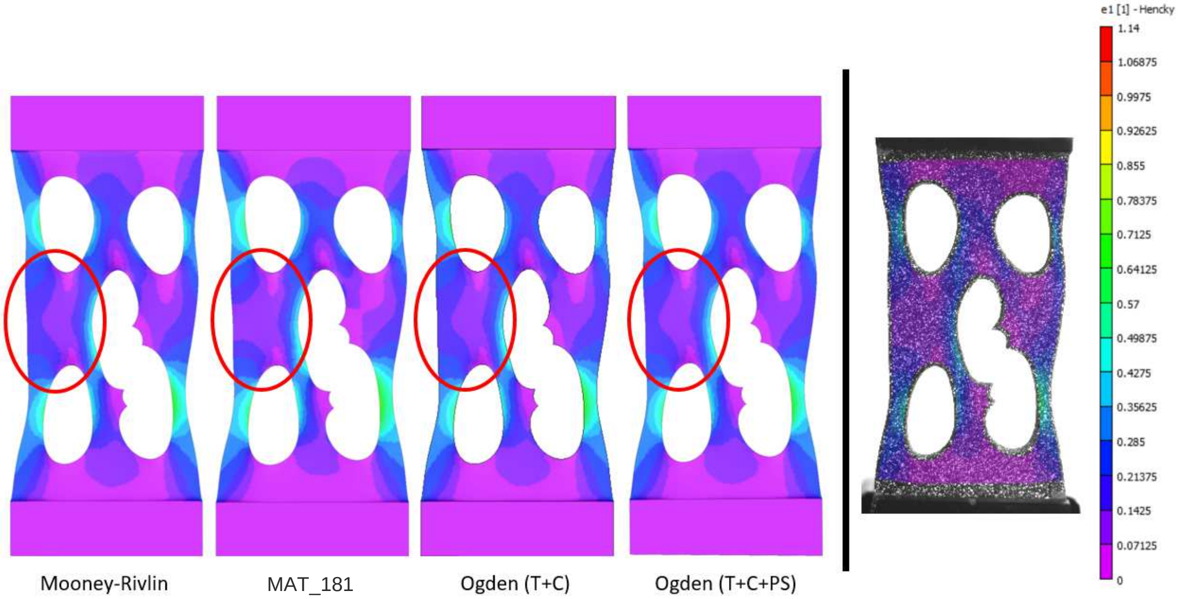

Figure 3.31: 6-HP 25% strain contour comparison

Contour plot comparisons of longitudinal principal strain were also made at a global strain of 50% (Figure 3.32). Again, the models other than the MAT_181 slightly over-predict the principal strain, most notably at the "hotspot" in the bottom right corner of the test sample. At this point, we see some separation between the accuracy of the Mooney-Rivlin and Ogden models, where the bottom right corner is slightly more red (higher principal strain) than the other tests. The MAT_181 does exceptionally well at replicating the validation test at this global strain.

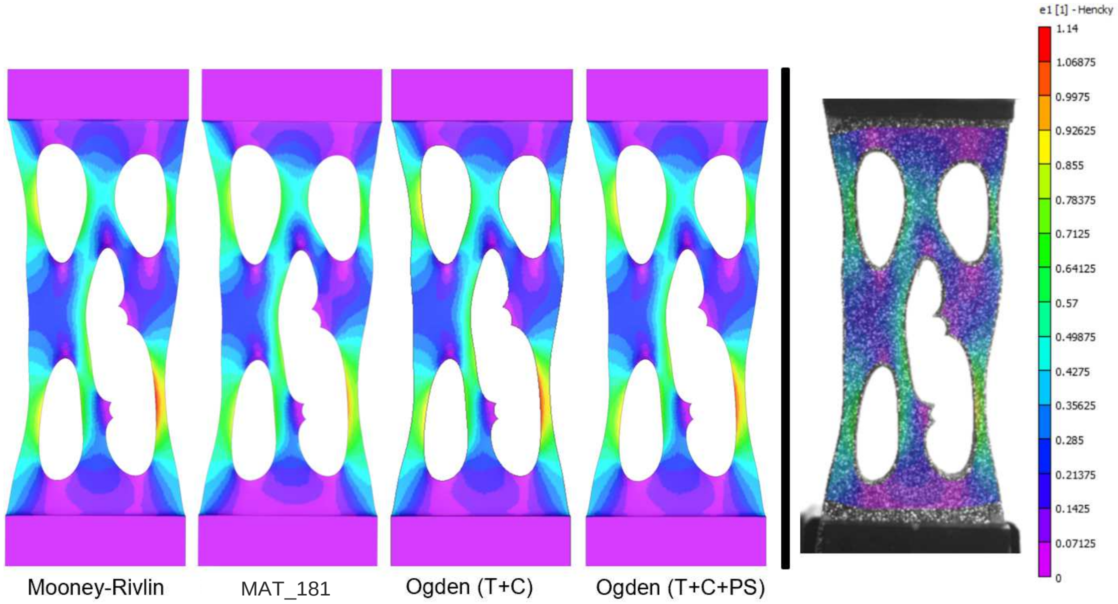

Figure 3.32: 6-HP 50% strain contour comparison

At the 75% strain level (Figure 3.33), we can see where the pure shear testing aids in the constitutive modeling development, where the "UTUC" over-calibrated the longitudinal principal strain more than the "UTUCPS" Ogden model does. The MAT_181 still best captures the maximum principal strain in all areas.

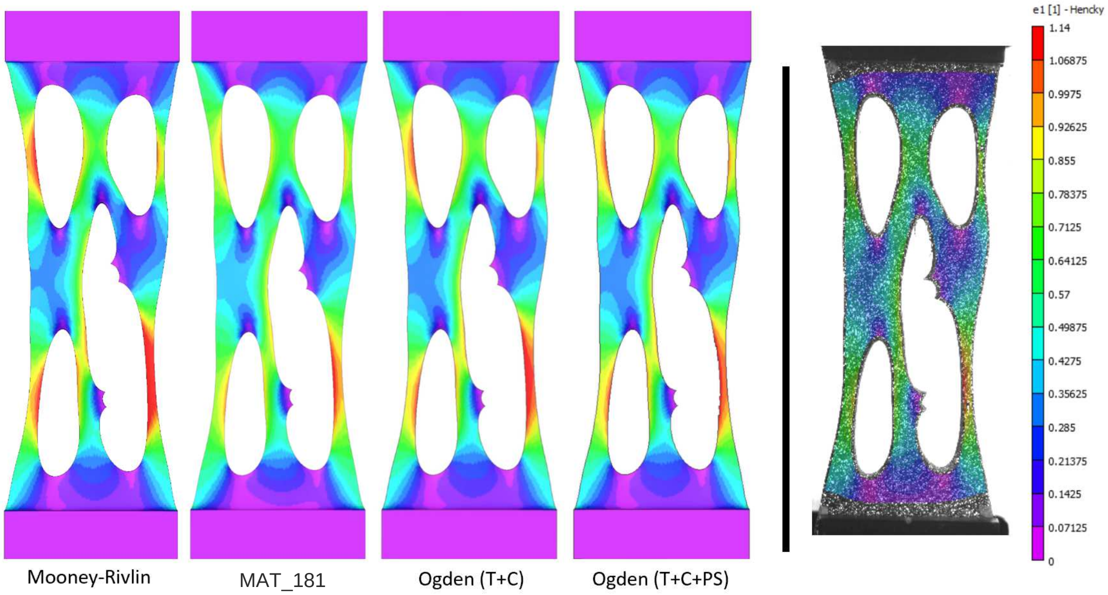

Mooney-Rivlin MAT_181 Ogden (T+C) Ogden (T+C+PS)

Figure 3.33: 6-HP 75% strain contour comparison

At the 100% strain level (Figure 3.34), we can see the expected continual increase in strain estimation, and where some error starts to form in the MAT_181. This model, however, still captures the strain contour very well. At this point in the simulation strains in each of the models start to exceed the legend of the validation test (maximized at 1.14 principal strain). As a result, further validation justification requires numerical comparison rather than visual.

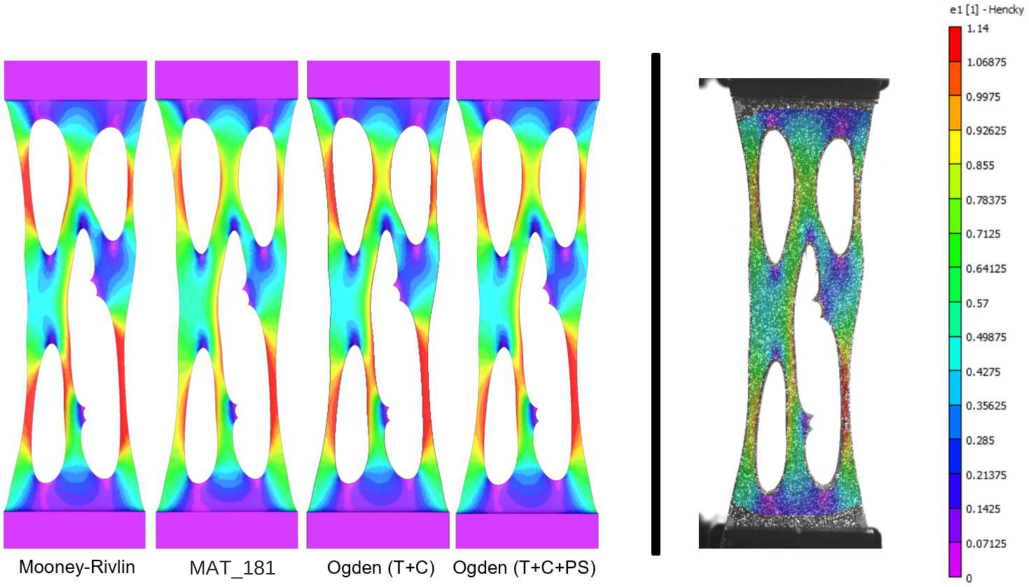

Figure 3.34: 6-HP 100% strain contour comparison

To numerically compare the constitutive models to the validation test, and further validate these material models, a virtual strain gauge was used, as described in Section 3.2.3. The virtual strain gauge was placed specifically in the "hotspot" in the bottom right of the contour plots, as this was an area where significant strain occurred, and where the test eventually fractured. To fully validate the models, data for transverse strain and force data were compared as well in Figure 3.35. We can see here that the Mooney-Rivlin drastically over-calculates a stiff stress-strain response for the force-displacement curve.

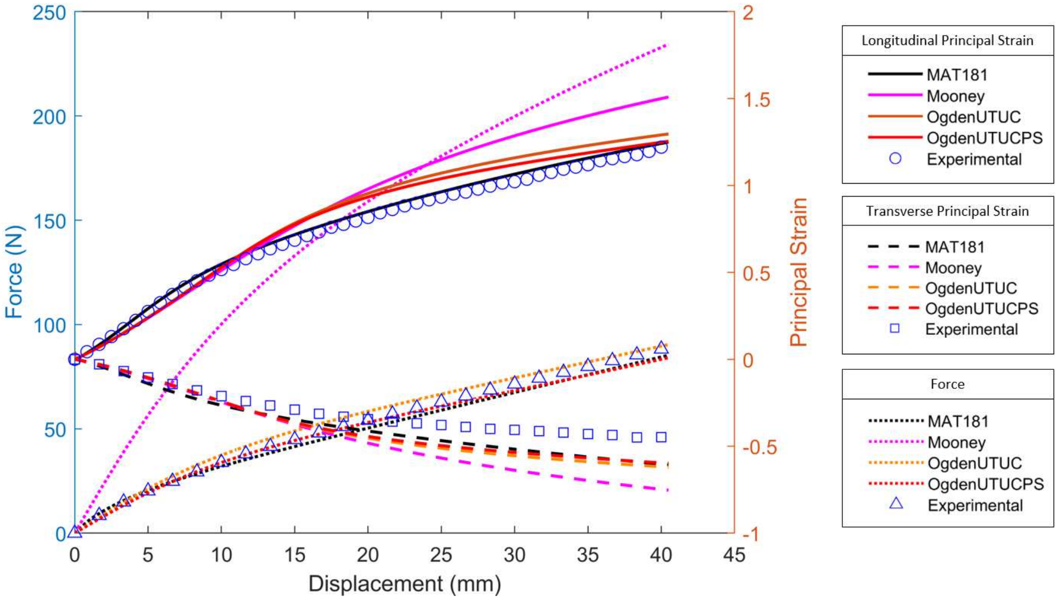

Figure 3.35: 6-HP validation

To better visualize the accuracy of the force-displacement plots in the other material models, another plot without the Mooney-Rivlin was produced in Figure 3.36. We can see that the MAT_181 best captures the shape of the experimental data in the principal strain plots. The MAT_181 nearly perfectly captures the longitudinal principal strain. The Ogden models are slightly worse, and it is worth noting the addition of pure shear testing in the constitutive model aided in replicating the strain softening seen in the experimental data. At early strains, the Ogden (UT+UC+PS) matches the force-displacement data the best but separates from the experimental data around the 20 mm mark. The MAT_181 is less effective in replicating the force response. There is some more error in the transverse principal strain direction (Table 3.7). The lack of implementation of simple shear testing into the constitutive models may have an impact on the ability of the model's ability to replicate the transverse strain in the experimental data.

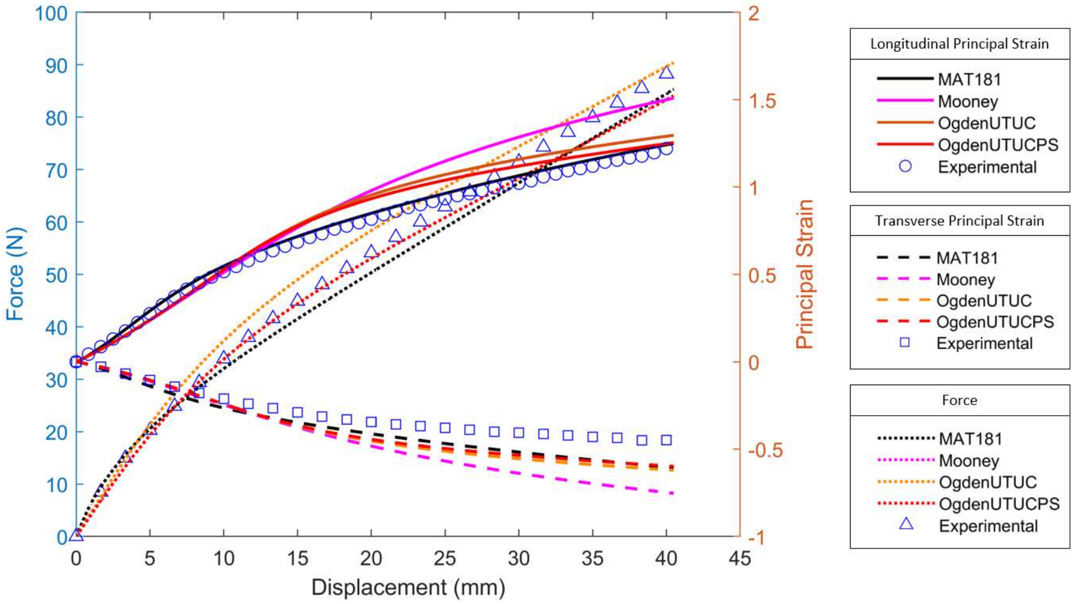

Figure 3.36: 6-HP validation

Table 3.7: 6-HP NRMSE

	MAT181	M-R	Ogden (UT+UC)	Ogden (UT+UC+PS)
Force	0.0380	0.0.4395	0.0345	0.0290
Longitudinal	0.0236	0.1222	0.0764	0.0602
Transverse	0.1450	0.2292	0.1862	0.1708

CHAPTER IV

CONCLUSIONS

4.1 Conclusions

Testing of potential sealant materials in Chapter II indicated that the Viton RB75A5 had the most desirable characteristics for this sealant application. Heat cycling resulted in increases in strength and decreases in elongation with modest heat cycling (20 cycles). Subsequent decreases in strength and increases in elongation were present with more extensive heat cycling (50 cycles). After 50 cycles, however, the material remains stronger than the unprocessed, virgin material.

The unconditioned Viton RB75A5 exhibited minimal viscoelastic effects in tension, with weak strain-rate sensitivity and only modest hysteresis in cyclic loading. A notable Mullins softening effect was observed during cyclic testing. The Mullins softening effect and thermal aging competed, causing simultaneous strain softening and stiffening. These viscoelastic and softening behaviors are important to consider in the desired sealant application as the material will often be repeatedly deformed at extreme temperatures. The validation tests confirm the fidelity of the coupon-level test data and the robustness of the calibrated constitutive models. The constitutive models for the unconditioned RB75A5 are validated and can be utilized in finite-element analysis to aid component design, optimization, and virtual testing.

4.2 Recommendations for Future Work

4.2.1 Materials

There are ever-changing versions of fluoroelastomers as they often come in compounds, as within this work, or they are often processed or manufactured in new ways, which can alter the material on a micro-structural level, leading to differences in the macro-mechanical properties. As a result, the work in this thesis could be repeated with other fluoroelastomer materials.

4.2.2 Experimental

Experimentally, I wished to perform stereo DIC on Viton seal compression tests. While the constitutive models are already validated and the simulation fulfills this need now, it would have added more brevity to the validation and would have been an interesting experiment to carry out. In addition, I think more development could be done on the experimental side. For example, if wide pneumatic grips are obtained, I think they would function well for a planar tension test, which may provide more repeatable and reliable results than the current mechanical test fixture, which was prone to specimen slippage. Due to the large specimen size and limited material, DIC was not attempted on pure shear testing, but this would be a great test to implement DIC to better obtain full-field strain measurements, not just length-averaged measurements between pairs of dots. Simple shear methods could be more repeatable, and would ideally induce cohesive failure (not adhesive). This could potentially provide better stress-stretch data for implementation into the Ogden constitutive model, which may help reduce the higher error in the transverse principal strain. Equi-biaxial tension is another experiment that would enhance the predictive capabilities of the constitutive model, but it would require custom fixtures that we do not currently have access to. Dynamic mechanical analysis (DMA) could be used to quantify mechanical properties as a function of time, temperature, frequency, or other external stimuli. Using scanning electron microscope (SEM) imaging could provide insight into fracture mechanics. In addition, only tension testing was performed at high-temperature, but all other tests could be performed at elevated temperatures with the appropriate equipment and environmental chamber.

4.2.3 Constitutive modeling

In this thesis, quasi-static tests were performed in uniaxial tension, uniaxial compression, pure shear, and simple shear. This data was used to calibrate three hyper-elastic constitutive models in the LS-DYNA material library: two parameterized (Mooney-Rivlin (MAT_027) and Ogden (MAT_077_O)), and one tabulated (MAT_181). This is a very limited set of the vast array of hyper-elastic constitutive models available in the literature [20, 21], many of which are more modern and offer attractive features. For instance, the Lopez-Pamies constitutive model was shown to reliably predict multi-axial stress states when calibrated to uniaxial tension data alone [37]. Implementing constitutive models not native to the LS-DYNA material library would require custom user material subroutines (e.g., UHYPER) written externally in Python or Fortran.

Uniaxial tension data at elevated temperatures was reported in this thesis for Viton RB75A5, however, this data was not incorporated into a thermo-hyperelastic constitutive model. The work of Alkhoury et al. [38], and references therein, are suggested as a template for an effort of this nature. In addition, fracture modeling can be implemented into the finite-element analysis of these materials, utilizing insight from Volokh [39].

In addition, cyclic load/unload testing was performed in both uniaxial tension and uniaxial compression. In both cases, the Mullins softening effect was prominent. For future work, it is recommended to incorporate this physics into the hyper-elastic constitutive models, which is often accomplished through the inclusion of a damage parameter [40]. From cyclic test data, the damage parameter can be derived and implemented into the Ogden and MAT181/MAT183 models [22]. A cyclic validation test was performed and achieved great correlation, which can be utilized as a baseline for validating the damage effects. Alongside this, it would have been interesting to delve into using the softened material (from the re-stretch portion of the cyclic test data) and fit hyper-elastic models to it (Ogden, Simplified Rubber), and do the same with a validation coupon (pre-stretch to the same strain), and see if the Ogden models better describe the softened material. We see the Ogden fit in Figure 3.20 has an N-like curvature similar to the re-stretch portion of the cyclic tension curve, indicating the curve-fitting optimization may effectively describe the softened material.

The validated constitutive models presented in this thesis have been implemented into seal compression simulations to analyze the mechanics of existing seal designs currently used in industrial manufacturing (Figure 1.3). These validated constitutive models can be used to simulate seal designs containing these fluoroelastomer materials at room temperature, and after further constitutive model development, thermally aged seals undergoing repeated loading and in high-temperature environments can be simulated.

BIBLIOGRAPHY

[1] Banerjee, S. S., Bhowmick, A. K. (2017). High-temperature thermoplastic elastomers from rubber–plastic blends: A state-of-the-art review. Rubber Chemistry and Technology, 90(1), 1–36. https://doi.org/10.5254/rct.16.83786

[2] Teng, H. (2012). Overview of the development of the fluoropolymer industry. Applied Sciences, 2(2), 496–512. https://doi.org/10.3390/app2020496

[3] Drobny, J. G.; Ebnesajjad, S. (2023). Technology of fluoropolymers: A concise handbook. CRC Press.

[4] Zhong, A. Challenges for High-Pressure High-Temperature Applications of Rubber Materials in the Oil and Gas Industry. In Proceedings of the Residual Stress, Thermomechanics and Infrared Imaging, Hybrid Techniques and Inverse Problems, 2016; Bossuyt, S., Schajer, G., Carpinteri, A., Eds.; Conference Proceedings of the Society for Experimental Mechanics Series; Springer International Publishing: Cham, Switzerland, 2016; Volume 9, pp. 65–79.

[5] Sharma, G., Klintberg, L.; Hjort, K. (2011). Viton-based Fluoroelastomer Microfluidics. Journal of Micromechanics and Microengineering, 21(2), 025016. https://doi.org/10.1088/0960-1317/21/2/025016

[6] Treloar, L.R.G.(1944): Stress-strain data for vulcanised rubber under various types of deformation. Trans. Faraday Soc. 40, 59-70.

[7] Meunier, L., Chagnon, G., Favier, D., Orgéas, L., Vacher, P. (2008). Mechanical experimental characterisation and numerical modelling of an unfilled silicone rubber. Polymer Testing, 27(6), 765–777. https://doi.org/10.1016/j.polymertesting.2008.05.011

[8] Nunes, L. C. S. (2010). Shear modulus estimation of the polymer polydimethylsiloxane (PDMS) using digital image correlation. Materials and Design, 31(1), 583–588. https://doi.org/10.1016/j.matdes.2009.07.012

[9] Nunes, L. C. S. (2011). Mechanical characterization of hyperelastic polydimethylsiloxane by simple shear test. Materials Science and Engineering: A, 528(3), 1799–1804. https://doi.org/10.1016/j.msea.2010.11.025

[10] Moreira, D. C.; Nunes, L. C. S. (2013). Comparison of simple and pure shear for an incompressible isotropic hyperelastic material under large deformation. Polymer Testing, 32(2), 240–248. https://doi.org/10.1016/j.polymertesting.2012.11.005

[11] Wanasinghe, S. V., Johnson, B., Revadelo, R., Eifert, G., Cox, A., Beckett, J., Osborn, T., Thrasher, C., Lowe, R., Konkolewicz, D. (2023). 3D printable adhesive elastomers with dynamic covalent bond rearrangement. Soft Matter, 19(26), 4964–4971. https://doi.org/10.1039/d3sm00394a

[12] Brown, R. H. (2018). Physical test methods for elastomers. In Springer eBooks. https://doi.org/10.1007/978-3-319-66727-0

[13] Treloar, L. R. G. (1943). The elasticity of a network of long-chain molecules—II. Transactions of the Faraday Society. 39: 241–246.

[14] Mooney, M. (1940). A theory of large elastic deformation. Journal of Applied Physics, 11(9), 582–592. https://doi.org/10.1063/1.1712836

[15] Gent, A. N. (1996). A new constitutive relation for rubber. Rubber Chemistry and Technology, 69(1), 59–61. https://doi.org/10.5254/1.3538357

[16] Yeoh, O. H. (1990). Characterization of elastic properties of carbon-black-filled rubber vulcanizates. Rubber Chemistry and Technology, 63(5), 792–805. https://doi.org/10.5254/1.3538289

[17] Arruda, E. M., Boyce, M. C. (1993). A three-dimensional constitutive model for the large stretch behavior of rubber elastic materials. Journal of the Mechanics and Physics of Solids, 41(2), 389–412. https://doi.org/10.1016/0022-5096(93)90013-6

[18] Ogden, R. W. (1972). Large deformation isotropic elasticity – on the correlation of theory and experiment for incompressible rubberlike solids. Proceedings of the Royal Society of London, 326(1567), 565–584. https://doi.org/10.1098/rspa.1972.0026

[19] Ogden, R. W. (1997). Non-linear elastic deformations. Courier Corportation.

[20] Steinmann, P., Hossain, M., Possart, G. (2012). Hyperelastic models for rubber-like materials: Consistent tangent operators and suitability for Treloar's data. Archive of Applied Mechanics, 82(9), 1183–1217. https://doi.org/10.1007/s00419-012-0610-z

[21] Hossain, M.; Steinmann, P. (2013). More hyperelastic models for rubber-like materials: Consistent tangent operators and comparative study. Journal of the Mechanical Behavior of Materials, 22(1–2), 27–50. https://doi.org/10.1515/jmbm-2012-0007

[22] LS-DYNA User Manual and Theoretical Manual, Livermore Software Technology

[23] Benson, D. J., Kolling, S., and Du Bois, P. A. (2006, June). A simplified approach for strain-rate dependent hyperelastic materials with damage. In 9th International LS-DYNA Users Conference (Vol. 15, pp. 29-36).

[24] Wang, S. (2018). Experimental characterization and continuum modeling of inelasticity in filled rubber-like materials. International Journal of Solids and Structures, 136–137, 125–136. https://doi.org/10.1016/j.ijsolstr.2017.12.010

[25] Feng, W. W., and Hallquist, J. O. (2014). Determining the Material Constants for Mullin Effect in Rubber Part One: Uniaxial. In 13th International LS-DYANA Users Conference (pp. 8-10).

[26] Feng, W. W., and Hallquist, J. O. (2016). Mullins Effect in Rubber Part Two: Biaxial. In 14th International LS-DYANA Users Conference.

[27] Mullins, L. (1969). Softening of rubber by deformation. Rubber Chemistry and Technology, 42(1), 339–362. https://doi.org/10.5254/1.3539210

[28] Bouaziz, R., Ahose, K. D., Lejeunes, S., Eyheramendy, D., Sosson, F. (2019). Characterization and modeling of filled rubber submitted to thermal aging. International Journal of Solids and Structures, 169, 122–140. https://doi.org/10.1016/j.ijsolstr.2019.04.013

[29] Smith, J. F., and Perkins, G. T. (1961). The mechanism of post cure of viton A Fluorocarbon elastomer. Journal of Applied Polymer Science, 5(16), 460-467.

[30] Kalfayan, S. H., Silver, R. H., Mazzeo, A. A., and Lui, S. T. (1972). Long Term Aging of Elastomers: Chemorheology of Viton B Fluorocarbon Elastomer. JPL Quart. Tech. Rev., 2(3).

[31] Abdihamzehkolaei, A., Ahad, M. T., and Siddique, Z. (2021). Volume Resistivity of Viton Polymer under Thermal Aging. Polymers, 13(5), 773.

[32] ASTM D412-16. “Standard Test Methods for Vulcanized Rubber and Thermoplastic Elastomers - Tension” ASTM International, West Conshohocken, PA. Reapproved 2021

[33] ASTM D575-91. “Standard Test Methods for Rubber Properties in Compression” ASTM International, West Conshohocken, PA. Reapproved 2018

[34] ASTM D1002-10. “Standard Test Method for Apparent Shear Strength of Single-Lap-Joint Adhesively Bonded Metal Specimens by Tension Loading (Metal-toMetal)” ASTM International, West Conshohocken, PA. Reapproved 2019

[35] International Digital Image Correlation Society. (2017). A Good Practices Guide for Digital Image Correlation. https://www.idics.org/guide/

[36] VIC-2D Digital Image Correlation Manual, Version 7.0. Correlated Solutions Digital Image Correlation https://www.correlatedsolutions.com/vic-2d/

[37] Lopez-Pamies, O. (2010). A new -based hyperelastic model for rubber elastic materials. Comptes Rendus Mécanique, 338(1), 3–11. https://doi.org/10.1016/j.crme.2009.12.007

[38] Alkhoury, K., Bosnjak, N., Wang, Y., Lee, H., Nadimpalli, S.; Chester, S. A. (2022). Experiments and modeling of the Thermo-Mechanically Coupled Behavior of VHB. International Journal of Solids and Structures, 242, 111523. https://doi.org/10.1016/j.ijsolstr.2022.111523

[39] Volokh, K. Y. (2010). On modeling failure of rubber-like materials. Mechanics Research Communications, 37(8), 684–689. doi:10.1016/j.mechrescom.2010.10.006

[40] Ogden, R. W. (1999). A pseudo-elastic model for the Mullins effect in filled rubber. Proceedings of the Royal Society of London. Series A: Mathematical, Physical, and Engineering Sciences, 455(1988), 2861-2877. doi:10.1098/rspa/1999.0431

APPENDIX A

LS-DYNA Material Cards

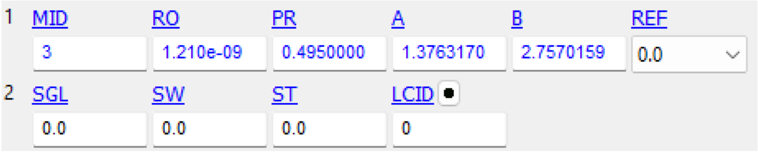

1	MID	RO	PR	A	B	REF
	3	1.210e-09	0.4950000	1.3763170	2.7570159	0.0
2	SGL	SW	ST	LCID ●		
	0.0	0.0	0.0	0		

Figure A.1: Mooney (MAT_027)) material card for uncured RB75A5

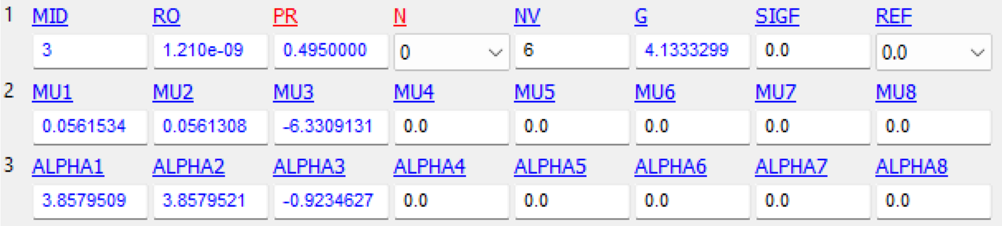

1	MID	RO	PR	N	NV	G	SIGF	REF
	3	1.210e-09	0.4950000	0	6	4.1333299	0.0	0.0
2	MU1	MU2	MU3	MU4	MU5	MU6	MU7	MU8
	0.0561534	0.0561308	-6.3309131	0.0	0.0	0.0	0.0	0.0
3	ALPHA1	ALPHA2	ALPHA3	ALPHA4	ALPHA5	ALPHA6	ALPHA7	ALPHA8
	3.8579509	3.8579521	-0.9234627	0.0	0.0	0.0	0.0	0.0

Figure A.2: Ogden UT+UC (MAT_077)) material card for uncured RB75A5

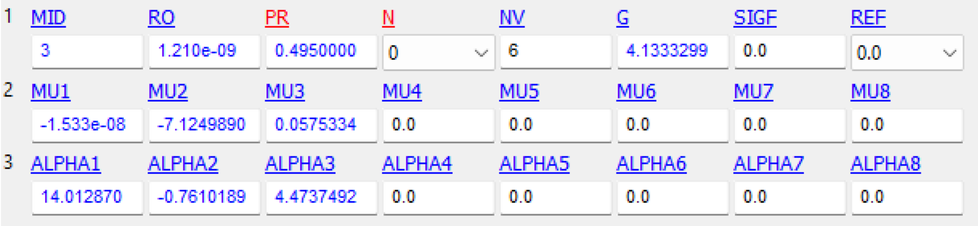

1	MID	RO	PR	N	NV	G	SIGF	REF
	3	1.210e-09	0.4950000	0	6	4.1333299	0.0	0.0
2	MU1	MU2	MU3	MU4	MU5	MU6	MU7	MU8
	-1.533e-08	-7.1249890	0.0575334	0.0	0.0	0.0	0.0	0.0
3	ALPHA1	ALPHA2	ALPHA3	ALPHA4	ALPHA5	ALPHA6	ALPHA7	ALPHA8
	14.012870	-0.7610189	4.4737492	0.0	0.0	0.0	0.0	0.0

Figure A.3: Ogden UT+UC+PS (MAT_077)) material card for uncured RB75A5

Note that "LC" below refers to a load curve defining the engineering stress (ordinate) vs. engineering strain (abscissa) in both tension in compression, provided in a single user-defined data set.

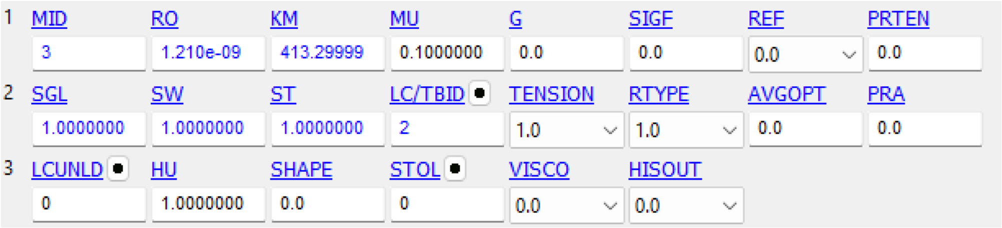

1	MID	RO	KM	MU	G	SIGF	REF	PRTEN
	3	1.210e-09	413.29999	0.1000000	0.0	0.0	0.0	0.0
2	SGL	SW	ST	LC/TBID ●	TENSION	RTYPE	AVGOPT	PRA
	1.0000000	1.0000000	1.0000000	2	1.0	1.0	0.0	0.0
3	LCUNLD ●	HU	SHAPE	STOL ●	VISCO	HISOUT		
	0	1.0000000	0.0	0	0.0	0.0		

Figure A.4: MAT181 for uncured RB75A5 - ch3